GEM TN-93-387

Pattern Recognition in the GEM Muon System

P. Dingus
Physics Research Department
Superconducting Super Collider Laboratory
Dallas, TX

June 29, 1993

Abstract;

A systematic monte carlo study of the ability of the proposed GEM Muon system to find and measure various types of muon tracks in the presence of both correlated and uncorrelated backgrounds is presented. A sample of 16000 isolated muon tracks with transverse momentum, $100 Gev \leq P_t \leq 1000 Gev$ and 4000 events from $t\bar{t} \Rightarrow b\bar{b} + \mu\mu\nu\nu \Rightarrow X + \mu\mu\nu\nu$ were simulated in the detector using the SIGEM[1] monte carlo, which was used in calculating GEM performance for the GEM TDR. Track reconstruction efficiencies and momentum resolution are calculated with respect to a given set of constraints that include the most basic performance assumptions underlying the architecture and technology choices made for the GEM muon system.

Pattern Recognition in the GEM Muon System

P. Dingus
Physics Research Department
Superconducting Super Collider Laboratory
Dallas, TX 75237

Abstract: A systematic monte carlo study of the ability of the proposed GEM Muon system to find and measure various types of muon tracks in the presence of both correlated and uncorrelated backgrounds is presented. A sample of 16000 isolated muon tracks with transverse momentum, $100Gev \leq P_t \leq 1000Gev$ and 4000 events from $t\bar{t} \Rightarrow b\bar{b} + \mu\mu\nu\nu \Rightarrow X + \mu\mu\nu\nu$ were simulated in the detector using the SIGEM[1] monte carlo, which was used in calculating GEM performance for the GEM TDR. Track reconstruction efficiencies and momentum resolution are calculated with respect to a given set of constraints that include the most basic performance assumptions underlying the architecture and techology choices made for the GEM muon system.

1 Introduction

There are two basic limitations that prevent the GEM muon system from reaching the quantitative limits of track reconstruction efficiency and track measurement resolution that one would naively calculate from just geometric acceptance and chamber resolution and chamber and superlayer alignment errors. The first problem is that of correlated and non-correlated track backgrounds such as punchthrough from the calorimeter, δ rays, γ conversions and random hits frome abient neutrons and γ's comming from neutron-nucleus interactions. The second, which only limits the momentum resolution are the fluctions in energy loss for relatively low momentum μ's passing through the calorimeter and the multiple scattering of muons in the material of the muon system. We will describe the nature of the correlated background associated with three files of isolated μ's of constant P_t distributed uniformly through out the detector and then with μ's in b jets coming from $t\bar{t}$ events. Finally we will, in the presence of these various correlated backgrounds, give track finding efficiencies and track reconstruction resolutions.

[1] Y.Fisyak GEM TN-162

2 Correlated Backgrounds

The correlated backgrounds include; δ rays produced by the μ on its passage through the material of the chambers, γ conversions due to γ's coming from μ bremsstrahlung both in the last few centimeters of the calorimeter and in the material of the μ chambers, and finally from charged punchthrough for non-isolated μ's.

In order to gauge the effect of associated charged particles on the track reconstruction efficiency we first look at the percentage of muon hits per strip layer that have an associated charged track close enough to the μ so as to spoil the resolution of the measurement.

The physical layout of the GEM μ chambers is shown in figure 1, as one can see the simulation is very detailed. Chambers contain aluminum supports, electronics blocks, and G10/copper readout boards. The average muon passing through the barrel muon system sees $0.5X_0$ of material while on occasion a muon can pass through chamber supports and see as much as $1X_0$ of material, this adds to multiple scattering and sets the lower limit on track measurement resolution for low momentum tracks.

In order to explore the effect of correlated background on track finding and fitting we will adopt the convention, by considering the single track resolution in the presence of another charged track within some distance of it, that a muon hit in a chamber plane can be compromised if it falls within the interval, $0.02cm \leq \Delta x \leq 2strips$, of another charged track. If the background hit is closer than 200 microns then we measure the double track as a single charged track. Also in the interest of brevity we will refer to the single track resolution in the presence of another track as the "two track" resolution. Figure 2 a, b, and c show the distributions of charged particle hits that come within Δx of the muon, in the direction of the strips, for each of the three superlayers for muon momentums 100 Gev P_t, 500 GeV P_t, and 1TeV P_t. Only one entry per event is plotted, corresponding to the charged hit which came closest to the muon. The barrel region is taken to be $0.1 \leq \eta \leq 1.2$, the endcap region is $1.25 \leq \eta \leq 2.5$. One sees that in the endcap the relative number of close correlated hits (the first bin of the plots) in the first superlayer dominates the numbers in the second and third superlayers for all P_t's, with the second superlayer busier than the third. For the barrel however, this is not the case. With no cut on the energy of the secondary hits in the barrel we see that in the 1TeV P_t sample there are only slightly more hits in the first superlayer than in the second or third, with the third having slightly more than the second. In figure 2b, the 500 GeV P_t sample, the first (dotted line) and second superlayers have equal occupancy in the bin closest to the muon and the third superlayer is busier. For the 100 GeV P_t sample, the trend has completely reversed with the first superlayer quieter than the second and the second quieter than the third. The reason for this trend is that the gas volume widths in the barrel increase with superlayer, the first superlayer has a gas gap width of about 0.5 cm while for the second and third they are 0.7 and 1.0 cm respectively. Many of the close secondary hits are due

to soft δ rays formed in the gas, which deposit anywhere from from 1 to 500KeV of energy in the gas. These can't be neglected since the muon deposits an average of 1 to 3 KeV of energy in the 0.5cm gas gap. Figures 3a and 3b show the energy of the secondary hits as a function of the radial position of the particle origin for the three superlayers, the verticle lines of points are secondary charged particles made in the G10/Cu cell boundry and the points inbetween are those produced in the gas. Figure 4 shows the effect on the barrel Δx distribution of the 1TeV sample of making a 500KeV cut, and a 1MeV cut. The first bin inverts its occupancy, i.e. the first superlayer is busier than the second, the second is busier than the third, while the bins farther from the muon are unchanged. Figures 5a and 5b show the origin of the extra hits in the gas layers in radial distance for the barrel and in z for the endcap, for the 1TeV sample. One sees that in the barrel the contribution to extra hits in the first superlayer due to charged particles whose origin is the calorimeter is less than 10% while in the endcap it is greater than 50%. Figure 6 shows the correlated occupancy per plane for the isolated 1 TeV muon events in the barrel, $0.1 \leq \eta \leq 1.4$, and endcap, $1.4 \leq \eta \leq 2.4$. The basic feature here is that in the barrel, the 20cm clearance between the top of the calorimeter and the closest part of the first muon superlayer is sufficient to all but eliminate charged particles created in the top layers of the calorimeter from reaching to within 2 strips of the muon on the first superlayer. This results from the fact that it would take a minimum of 50.0 MeV of P_t for a charged particle created at the top of the calorimeter to reach the first muon superlayer and about 500.0 MeV of P_t for a charged particle leaving the top of the calorimeter in the direction of the muon, and leaving the calorimeter from the same point as the muon, to hit the first plane of the muon system to within 1.0 cm (two strips) of the muon. In figures 7a and 7b be seen the energy distributions of e^+ and e^- correlated to the muon and exiting the top of the calorimeter that 500 MeV charged particles are well on the tail of the distributions and contribute no more that 1% or 2% to the background. In the endcap region however this is not the case. The momentum magnitude of muons at $\theta = 20^0$ is a factor of 3 larger than those having the same P_t at $\theta = 90^0$, thus these muons tend to shower more in the endcap. Also the magnetic field in the endcap actually sweeps charged particles in the direction of the field, i.e. soft particles have a helicital trajectory around the magnetic field lines in the direction of the endcap chambers, thus causing a higher occupancy of background hits in the first superlayer of the endcap.

Another major source of background are γ conversions from γ's bremsstrahlung by the high energy μ's. At about 700 GeV muon energy loss by bremsstrahlung is equal to that by ionization, therefore high energy μ's tend to radiate photons whose direction is close to that of the muon. Figure 8a shows the energy distribution of γ's of 1 TeV muons emerging from the calorimeter with $\theta = 60^0$ and $\phi = 6^0$ while figure 8b shows their angular distribution. If one takes the opening angle required to intercept the second muon superlayer to within two strips of the muon, ± 1.4 cm, and the same for the third superlayer, ± 2 cm, then the dark region of figure 8 represents the excess in hits due to conversions on superlayer 2 over superlayer 3, in the barrel. This should be less than

10%. Also if one takes the mean free path between interactions for 10 MeV γ's in 0.5 X0 of G10, one finds that the number of γ's available to convert on superlayer 3 relative to superlayer 2 is about 70%. For the 1 TeV sample of 1500 events in the barrel we measure;

$$\frac{N_{conversion}(SL3)}{N_{conversion}(SL2)} = 15/25 = 0.6 \tag{1}$$

which is consistant with our prediction, since for these numbers the ratio has a $\pm 20\%$ error.

The percentage of spoiled planes per superlayer for both δ rays and conversions are tabulated in Table 1 for all three P_t samples. Note that if one were to assume all hits on the individual chambers of a superlayer to be independent then, for example; if one takes the average plane occupancy from figure 6 for the 1TeV P_t sample in the barrel to be $\sim 7\%$, then 0.93^6 should be the percentage of planes in Table 1 seen to have "0" spoiled planes for superlayer 1. This yeids $0.93^6 = 0.646$, the Table 1 entry is 0.624. Futher if one assumes the superlayers are independent and if one were to require 3 unspoiled planes per superlayer to constitute a track segment then for the 1 TeV P_t sample the track finding efficiency for this simple senario would be $0.976 \times 0.989 \times 0.986 = 0.95\%$. The same simple calculation can't be made in the endcap since there, there are many correlated spoiled planes.

Table 1, Compromised Plane Distributions

Detector	Barrel			Endcap		
Superlayer	1	2	3	1	2	3
Plane	Compromised Plane Probability, 100 GeV.					
0	0.689	0.654	0.606	0.597	0.704	0.737
1	0.930	0.909	0.880	0.819	0.899	0.91
2	0.988	0.981	0.992	0.912	0.961	0.966
3	0.998	0.997	0.998	0.948	0.979	0.982
4	0.998	0.999	0.999	0.964	0.989	0.988
5	1.0	0.999	1.0	0.977	0.994	0.994
6	1.0	1.0	1.0	0.984	1.0	1.0
7	-	-	-	0.989	-	-
8	-	-	-	1.0	-	-

Detector	Barrel			Endcap		
Superlayer	1	2	3	1	2	3
Plane	Compromised Plane Probability, 500 GeV.					
0	0.642	0.565	0.540	0.528	0.670	0.70
1	0.917	0.919	0.882	0.749	0.893	0.91
2	0.968	0.984	0.974	0.832	0.948	0.955
3	0.986	0.994	0.993	0.874	0.973	0.974
4	0.992	0.996	0.996	0.906	0.984	0.978
5	0.995	0.999	0.996	0.932	0.991	0.989
6	1.0	1.0	1.0	0.949	1.0	1.0
7	-	-	-	0.963	-	-
8	-	-	-	1.0	-	-

Detector	Barrel			Endcap		
Superlayer	1	2	3	1	2	3
Plane	Compromised Plane Probability, 1000 GeV.					
0	0.624	0.564	0.542	0.521	0.657	0.693
1	0.871	0.866	0.859	0.705	0.867	0.883
2	0.953	0.963	0.960	0.781	0.939	0.939
3	0.976	0.989	0.986	0.821	0.965	0.964
4	0.986	0.994	0.994	0.858	0.974	0.980
5	0.993	0.997	1.0	0.886	0.987	0.987
6	1.0	1.0	1.0	0.910	1.0	1.0
7	-	-	-	0.928	-	-
8	-	-	-	1.0	-	-

3 Track Reconstruction Efficiency

An upper limit to the track reconstruction efficiency can be set by requiring at least three "good" hits per superlayer in each of the three muon superlayers for an event. A good hit is defined as one where, with respect to the two track resolution, a background δ ray or conversion γ is either too close or too far from the muon to spoil the resolution of the measurement, this is consistent with our definition of the "standard interval". One can see that if we have 3 such good hits in a superlayer then we can find a line segment fit to these 3 hits with residuals between this line and the hits that approximate the chamber resolution. In fact one could probably do better than this by using the hits in the third superlayer to establish a track stub for some global iterative fit, such as a Kalman filter, and then picking up successive points on the trajectory and weighting these points by the

measurement error according to the two track resolution. This has been done, and will be disscussed below. The track finding efficiencies for isolated muons can be seen in figure 9.

We developed a track finding algorithm that is described in detail in GEM TN-93-416. We will not attempt to describe the fine points of the methode here but will concentrate more on the results. The original idea with the "three point" methode discribed above and shown in figure 9 was to demonstrate the canonical track finding potential of any good track finding algorithm given the physical parameters of the GEM muon system. The number of points used in any senario, like the one above where we use 3 good points in each superlayer, must be determined in such a way as optimize the track finding efficiency and at the same time to minimize the number of fake tracks reconstructed via random hits and conspiracies due to punchthrough charged particles.The fake track calculation was based on a road through 3 superlayers assuming the number of strips on each superlayer which would fully contain the track if the following procedures and conditions were met. A track is found by first establishing a bend plane cluster of charged hits on the third superlayer. Then a line is fit to this cluster and is projected to the second superlayer. If a cluster can be found on the second superlayer, in the vicinity of the third superlayer projection, whose best fit line forms an angle of intersection with that of the previous superlayer cluster of $\theta = 2.0cos^{-1}(\frac{0.3BL}{2P_t}) \geq 170^0$, the track segments will be merged. The procedure is continued so as to form a track from clusters on each of the three superlayers that can be merged in this way. This procedure implies the following road for a 10 GeV track in the barrel of the GEM muon system; 4 strips on the third superlayer, 40 strips on the second superlayer, and 77 strips on the first superlayer. This is consistant with a 10 GeV muon track of $\pm$ charge coming from the IP and being found in the way discribed above. If one assumes an average occupancy of 0.6%[2] of random hits per chamber strip from γ's and neutrons for a 600 ns DAQ time, one finds the probability of a fake track in a 10 GeV road to be about 2×10^{-6} if a minimum of three good hits are taken per track segment per superlayer. We ran the track finding algorithm on the sample of events where three "good" hits per chamber (plane) had already been selected so as to find the decrease in efficiency imposed due to the added constraints of the track finding algorithm over just finding 3 good hits per superlayer by information given by the simulation. The ideal efficiency as a function of η can be seen in figure 9 for three P_t ranges. The comparision between the ideal and the track finding algorithm is seen in figure 10 and shows this algorithm produces the same efficiency as the ideal to within 1%, which is about the error on the efficiency given our statistics. We then calculated the number of fakes in the same road, with the same occupancy and DAQ time, for a senario of (2,2,4) good hits on the $(1^{st}, 2^{nd}, 3^{ird})$ superlayers respectively. This senario is attractive since the first superlayer is the busiest in terms of non-muon activity coming from the calorimeter while the 3^{ird} is the quietest, especially in the endcap. The rate of fakes from from the (2,2,4) senario is about a factor of 10 less than that for the (3,3,3), thus we use either of these two senarios

[2]this is the rate quoted in the GEM TDR

as a condition for merging the tracks. We find an increase in efficiency of about 1% to 3%, the results are tabulated below. Senario 1 refers to (3,3,3), senario 2 refers to (2,2,4), and T.F. refers to track finding algorithm.

100 GeV P_t Isolated muons.			
η	3 good	T.F. (senario 1)	T.F. (senario 1+2)
0.08-0.5	0.9836	0.9779	0.9866
0.5-0.92	0.978	0.974	0.9846
0.92-1.34	0.965	0.959	0.9714
1.38-1.86	0.952	0.925	0.9598
1.86-2.46	0.9412	0.915	0.9594

500 GeV P_t Isolated muons.			
η	3 good	T.F. (senario 1)	T.F. (senario 1+2)
0.08-0.5	0.9757	0.971	0.9807
0.5-0.92	0.966	0.9598	0.9683
0.92-1.34	0.9488	0.941	0.9547
1.38-1.86	0.9148	0.898	0.9415
1.86-2.46	0.89	0.874	0.9215

1000 GeV P_t Isolated muons.			
η	3 good	T.F. (senario 1)	T.F. (senario 1+2)
0.08-0.5	0.9581	0.948	0.9714
0.5-0.92	0.9643	0.956	0.9648
0.92-1.34	0.9212	0.909	0.9488
1.38-1.86	0.8764	0.845	0.8935
1.86-2.46	0.8367	0.81	0.8475

Examples of found clusters and merged tracks are shown in figures 11.

3.1 Muons in b Jets

In order to understand the differences in track reconstruction efficiency in quite and noisy enviroments we prepared a sample of 4000 events of muons coming from b jets. These events were generated via Pythia as follows:

$$t\bar{t} \Rightarrow b\bar{b} + X \tag{2}$$
$$\Rightarrow b \rightarrow \mu^- \bar{\nu} + X \tag{3}$$
$$\Rightarrow \bar{b} \rightarrow \mu^+ \nu + X \tag{4}$$

The same, "three good hit", analysis was performed on these events as on the isolated sample. Very low physics cuts, 10 kev on all electromagnetic processes, were used in processing these events through the simulation so that the the background transport was as it was in the isolated sample. In order to get good statistics only that part of the event relevant to the muon was fully simulated. The procedure was to find the μ's in the event after the generator and before the simulation and to record those μ's whose ancestors were B mesons. Once these were found a cone of $r = \sqrt{\Delta\eta^2 + \Delta\phi^2} = 1.0$ was formed around the muon and all particles whose $E > 3.0GeV$ were processed through the simulation. There are on average 64 particles in a cone close to the muon. The average energy of these particles in the barrel is $\sim 50GeV$ and $\sim 162GeV$ in the endcap. This is seen in figures, 12a to 12f. It was found that the hadronic punchthrough from the calorimeter is negligable, $\sim 1\%$ of the events had hadronic punchthrough which came within the Δx interval defined above. The distribution of background hits is seen in figure 13. The energy spectrum of the μ's from b's is considerably softer than that of the 100 GeV P_t sample and so it is natural to compare the track finding efficiencies of the isolated 100 Gev P_t sample with that of the muon sample from b jets. This comparison is shown in figure 14. One sees that both samples have efficiencies $> 93\%$ over the entire η range from $\eta = 0.1$ to $\eta = 2.45$ with $\epsilon \geq 96\%$ for both samples in the barrel. The μs from b jets have greater track finding efficiencies by $\sim 1\%$ in the barrel and $\sim 1.5 - 2.0\%$ in the endcap than the isolated 100 GeV P_t sample.

3.2 Track Fitting

Finally an attempt was made to fit tracks that could be found as described above, i.e. tracks that had at least 3 "good" hits per superlayer. The technique that was choozen was that of Kalman filtering. The advantage of this system is that it fits to each consecutive point on the track by an estimate of the previous fitted points and their χ^2 errors. Thus track projections can be made which search for track stubs through bulk matter such as the calorimeter where no track information may be available or in cases where superlayers are missing in the muon system itself.

The implimentation of the Kalman filter was based on the Geane tracking package which has been adapted to use the Geant volumes, materials, and magnetic field banks used by the GEM simulation, in this case the SIGEM simulation of the GEM detector. The Geane package given information, about the measurement error on space points and track segment slopes produced by hits in the muon system superlayers and two unit vectors lying in the CSC measurement plane of each hit, will swim the trajectory parameters of the track to seccessive measurement planes. It also provides a tracking covariance matrix, from its knowledge of the materials, that discribes the multiple scattering and energy loss, using a gaussian approximation, of muons swimming between measurement planes. In

this implimentation we have taken the tracking vector to include; $(\frac{1}{p}, v\prime, w\prime, v, w)$. These five parameters uniquely define a track, they are defined as follows:

- $\frac{1}{p}$ is the curvature of the track.
- $v\prime$ is the slope of the track in a plane containing the unit vector in the measurement plane, v, and the unit vector normal to the measurement plane, u, where (u, v, w) form an orthonormal local coordinate system for the current measurement plane.
- $w\prime$ is the same as $v\prime$ but in the (u, w) plane.
- v is the v component of the hit on the local measurement plane, this direction is taken as the CSC strip direction of the CSC chamber.
- w is the w component of the hit on the local measurement plane and is taken as the wire direction of the CSC chamber.

The Kalman filter minimizes the following χ^2 :

$$\chi^2 = \sum_{i}^{planes} (x_i - \theta)^T V_i^{-1} (x_i - \theta) + (P_i - \theta)^T W_i^{-1} (P_i - \theta) \tag{5}$$

where :

- x = vector of measured track parameters.
- θ = fitted vector of track parameters.
- P = predicted vector of track parameters.
- V = measurement covariance matrix.
- W = Tracking covariance matrix.
- $\sigma = \sigma^2$, this definition is made so as not to overly burden the notation.
- i = measurement plane index.

Geane provides the following facilities;

$$P_i = F_{i,i-1}\theta_{i-1} \tag{6}$$
$$\sigma_{P_i} = T_i^T \sigma_{\theta_{i-1}} T_i + W_i \tag{7}$$

These two equations represent first the perdiction of the track parameters on plane i given their values on plane i-1, and second the tracking covariance matrix of the predicted values on plane i. In the above formula $F_{i,i-1}$ swims the track parameters between planes i and i-1 and $T_i = \dot{T}_{i,i-1}$ is the transport matrix between planes i and i-1 defined as;

$$T_i = \frac{\partial P_i}{\partial \theta_{i-1}} \tag{8}$$

The Kalman filter proceeds in two steps, first it loops over all the hit planes in a track candidate. This is the filter step where it makes a first estimate of the fitted track vector, $\bar{\theta}_i$ and the associated covariance matrix:

$$\bar{\theta}_i = \sigma_{\bar{\theta}_i}(\sigma_{P_i}^{-1} P_i + V_i^{-1} x_i) \tag{9}$$
$$= \frac{(\sigma_{P_i}^{-1} P_i + V^{-1} x_i)}{\sigma_{\bar{\theta}_i}^{-1}} \tag{10}$$
$$\sigma_{\bar{\theta}_i}^{-1} = \sigma_{P_i}^{-1} + V_i^{-1} \tag{11}$$

Notice that the initial estimate of track parameters is just the weighted mean of the predicted and measured track parameters. Once the filtering is done we loop through all the planes a second time in the reverse order to that of the filtering so as to use information about the fitted and perdicted track vectors on the next plane, i+1, to corrected the fitted value on plane i. This is called smoothing, and is done in the follow iterative way;

$$\theta_i = \bar{\theta}_i + A_i(\theta_{i+1} - P_{i+1}) \tag{12}$$
$$\sigma_{\theta_i} = \sigma_{\bar{\theta}_i} + A_i(\sigma_{\theta_{i+1}} - \sigma_{P_{i+1}})A_i \tag{13}$$

where:

$$A_i = \sigma_{\bar{\theta}_i} T_{i+1} \sigma_{P_{i+1}}^{-1} \tag{14}$$

The final fitted track values are those given by θ_1 at the end of the smoothing loop between measurements $N \rightarrow 1$. The fit has been found to converge in two such filtering and smoothing iterations. The χ^2 and χ^2 probability of a typical fit to the 1 TeV P_t data including background is shown in figure 15b.

Alignment errors were factored into the fit by generating random numbers for each event such that the intersuperlayer alignment in the direction of the strips was smeared by a gaussian with sigma = 0.0025 cm. The same was done within each chamber in a superlayer, the chamber-chamber alignment was smeared by a gaussian with sigma = 0.005 cm in the direction of the strips and smeared by a uniform distribution of +/- 5.0 cm in the wire direction.

Local slopes were calculated from track segments found in each superlayer, and the error on the slope was found to be between 0.5 and 0.7 mrad depending on the number of points used to calculate the slope. The error on the measured corrdinate in the direction of the strips was set to $75\mu m$, which is the nominal chamber resolution. Other runs were made using different resolutions as a function of superlayer and angle between the track and the chamber wire, but the curves given in this paper are for $75.0\mu m$ resolution of the chambers and facilitate comparisons with other calculations that have been done.

The result of the fits can be seen in figures 16 to 18. Each figure shows three curves, one is a fit with only the hits due to the passage of the muon through the measurement plane with all the appropriate resolutions applied, these are represented by solid dots. They should be compared to with the parameterized curves of upward pointing triangles. The disagreement is about 1% overall, with the resolution given by the Kalman being larger than that of the MIT[3] parameterization. For the 100 GeV P_t sample, all of the support structures between superlayers and the aluminum support structures for the chambers were taken out of the simulation in order to compare to the MIT parameterization. Also, unlike the rest of the simulated data, this data sample was produced by scanning in η but shooting the μ's through the middle of a measurement plane ($\phi = 6^0$) so as to only go through one ϕ projective set of superlayers. The superlayers in both the barrel and endcap are staggered in the outward going direction of the muon track as a function of ϕ, thus upon changing ϕ sectors a muon track can change its effective lever arm through the magnetic field. Makeing this comparison at 100 GeV P_t shows at most a 0.5% difference in resolution.

Finally, we introduced correlated background from the simulation into the fit by using the two track resolution function to establish the measurement weight in the fit. We broke up the interval around the μ hit in a CSC plane, in the direction of the strips, into three regions. First, if a secondary charged hit was detected within 0.02 cm of the muon we considered this double track indistinquishable from a single track, thus the measurement weight for this hit was given as the single track resolution. Second, if another charged

[3] As given on p4-30 of the GEM TDR (L.Rosenson).

track was found in an interval between 0.02 and 0.05 cm of the muon hit, this hit was exclude from the fit since our ability to distinguish the charge centroid in this case is very bad, i.e. the resolution is about 1mm. Third, the interval between 0.05 cm and 2 strip widths, here we give the measurement weight as the "two track" resolution of figure 19. If a second charged track is registered outside of 2 strip widths of the muon we consider the muon hit to be uncompromised and the single track resolution is applied. The fitted resolution distributions and the corresponding fit qualities are shown in figure 20 for the 100 GeV P_t sample without background, structures, and in a single ϕ bin. The same distributions are shown in figures 15a and 15b for the 1 TeV sample with full background, structures, and ϕ averaging over the full 2π slices of the detector.

One can see that the effect of the backgound is to degrade the resolution by between 0.5% and 1% of the background free resolution on the average and can in some cases degrade it by as much as 2%. The fit has been run with many different intial conditions, that is different guesses of the initial momentum, momentum error, local slope, slope error, and two different data sets. The percision of the results seems to be about $\pm 0.5\%$ when the fit is tuned to give a good overall χ^2 distribution like the ones seen in figure 20.

Resolution as determined by Kalman Filter

Muon tracks without background.

η	$0.1 < \eta < 0.5$	$0.5 < \eta < 1.0$	$1.0 < \eta < 1.25$	$1.25 < \eta < 1.5$
P_t	Resolution in σ of $\frac{\Delta P_t}{P_t}$, no background.			
$100GeV$	0.0167	0.0155	0.0226	0.0265
$500GeV$	0.0573	0.0595	0.0633	0.0613
$1000GeV$	0.0938	0.0895	0.1050	0.1307

η	$1.5 < \eta < 1.84$	$1.84 < \eta < 2.0$	$2.0 < \eta < 2.5$
P_t	Resolution in σ of $\frac{\Delta P_t}{P_t}$, no background.		
$100GeV$ [4]	0.0242	0.0261	0.0304
$100GeV$	0.0288	0.0428	0.0395
$500GeV$	0.0843	0.1050	0.099
$1000GeV$	0.1573	0.1983	0.2079

Muon tracks with correlated background.

η	$0.1 < \eta < 0.5$	$0.5 < \eta < 1.0$	$1.0 < \eta < 1.25$	$1.25 < \eta < 1.5$
P_t	Resolution in σ of $\frac{\Delta P_t}{P_t}$, with background.			
$100GeV$	0.0171	0.0156	0.0237	0.0274
$500GeV$	0.0576	0.0617	0.0782	0.0764
$1000GeV$	0.0961	0.1079	0.1122	0.1524

η	$1.5 < \eta < 1.84$	$1.84 < \eta < 2.0$	$2.0 < \eta < 2.5$
P_t	Resolution in σ of $\frac{\Delta P_t}{P_t}$, with background.		
$100GeV$	0.0304	0.0430	0.0424
$500GeV$	0.090	0.1175	0.1150
$1000GeV$	0.1644	0.2042	0.2205

[4] Resolution determined without supporting structures for the muon chambers and superlayers

MATERIALS – 1.9 CM NOMEX
– 0.5, 0.7, 1.0 CM $CF_4 CO_2$ (SL 1,2,3)
– 0.05 CM G10
– 0.0017 CM Cu

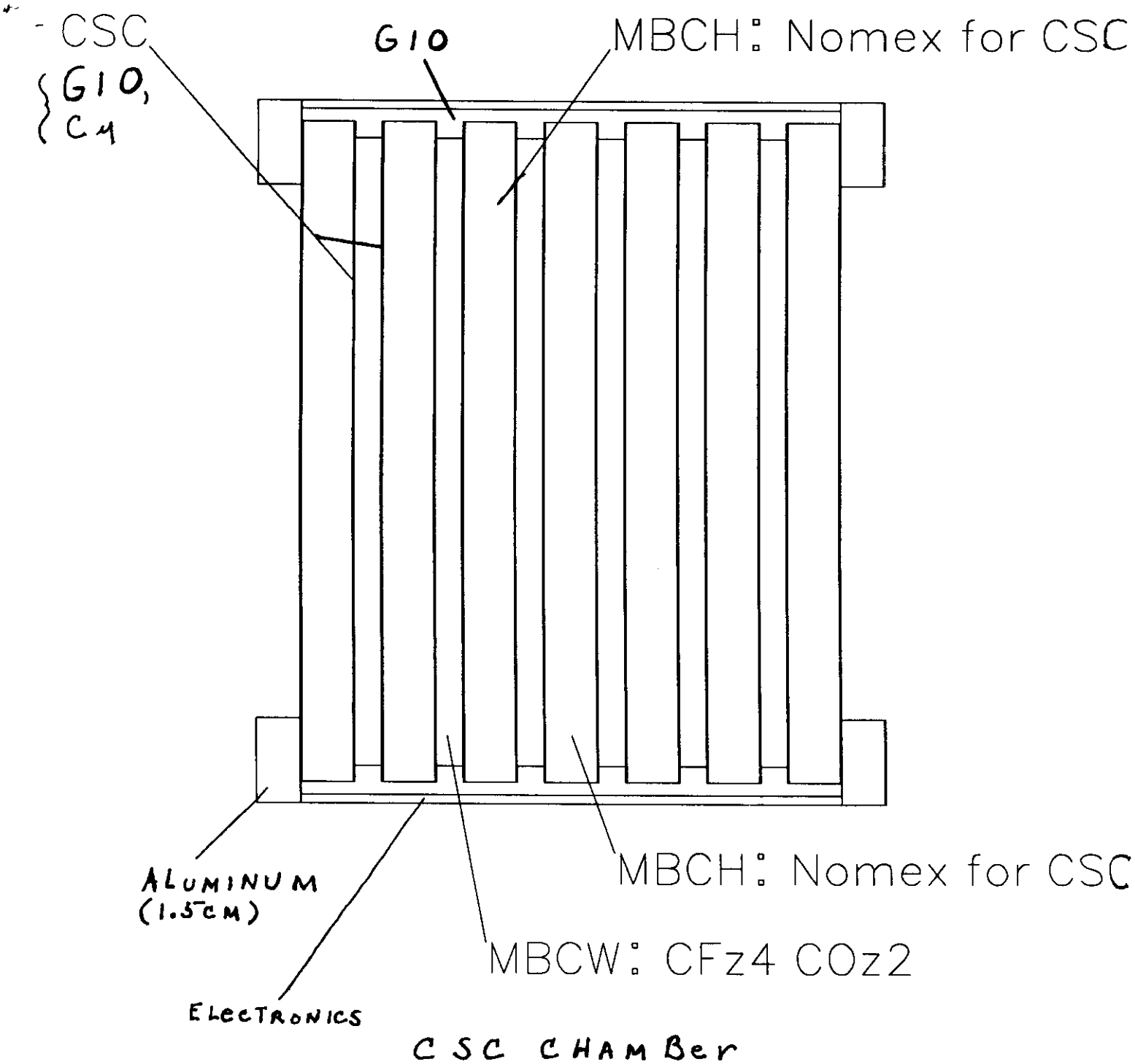

Figure 1) CSC chamber layout.

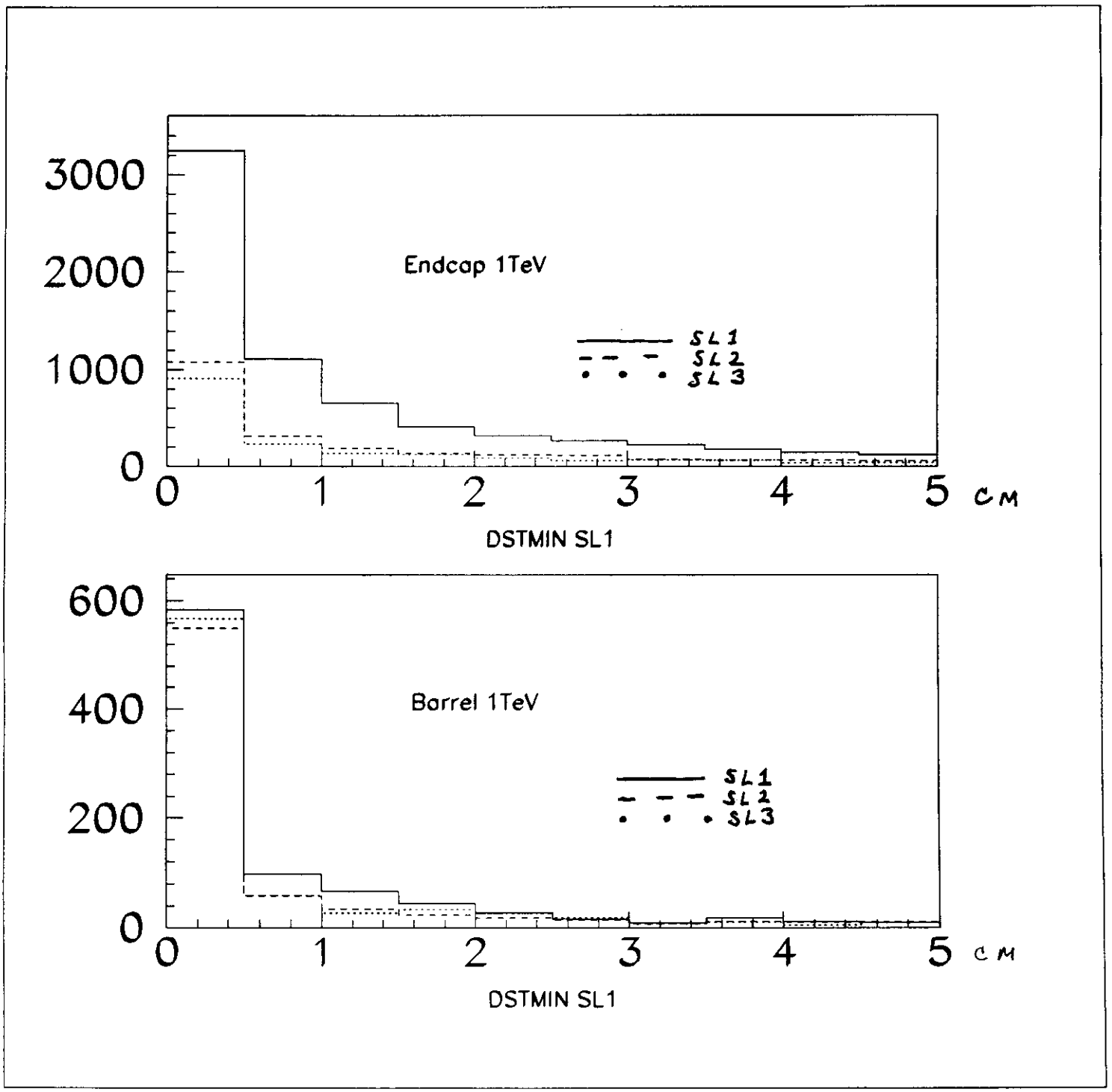

Figure 2a) Δx distributions of charged background hits around the muon in barrel and endcap for the 1 TeV event sample.

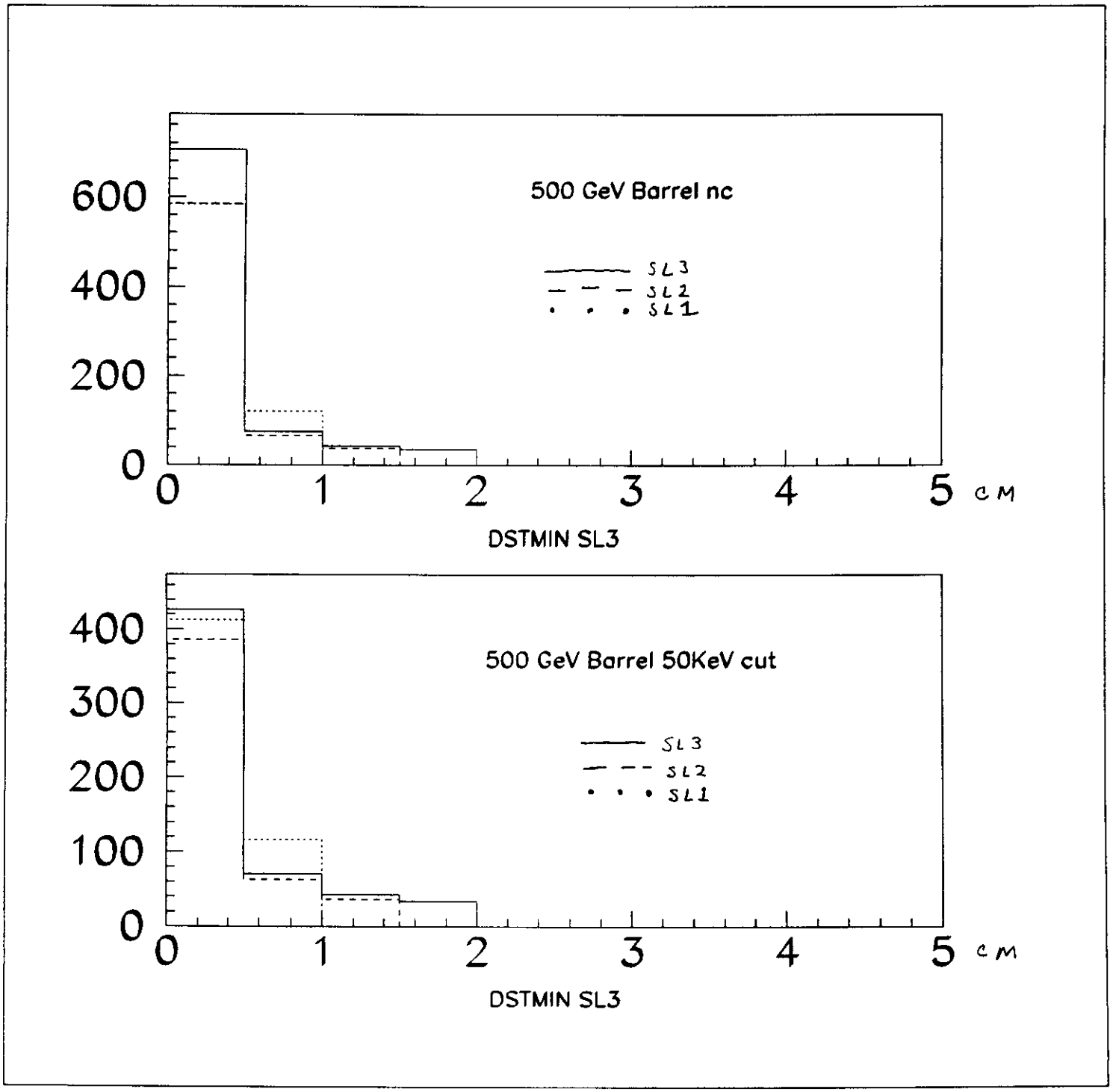

Figure 2b) Δx distributions of charged background hits around the muon in the barrel for the 500 GeV event sample. The second plot shows the dependence of the population of the first bin on the energy of the charged background. Note that the solid lines correspond to the 3^{ird} superlayer.

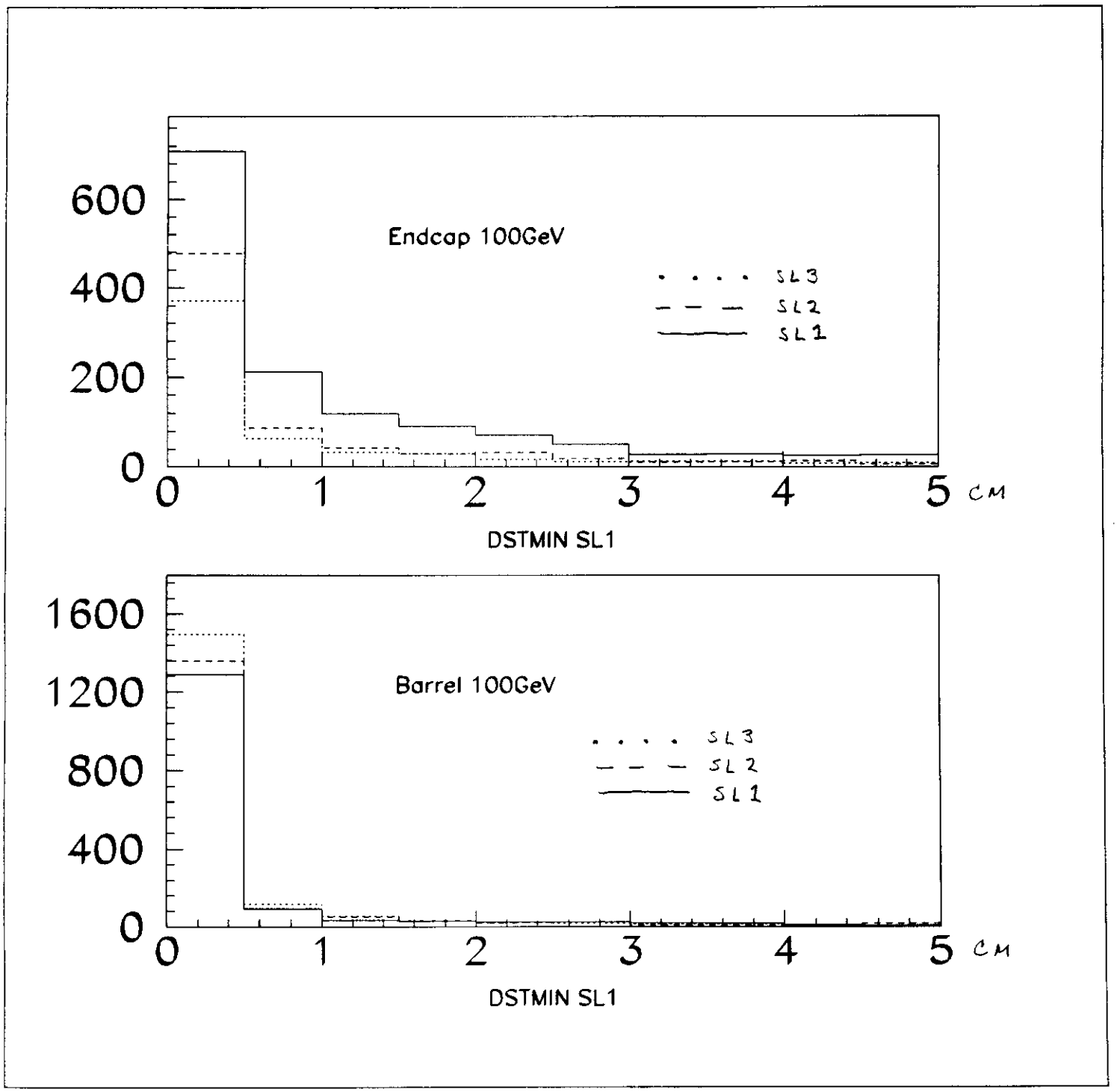

Figure 2c) Δx distributions of charged background hits around the muon in the barrel and endcap for the 100 GeV event sample.

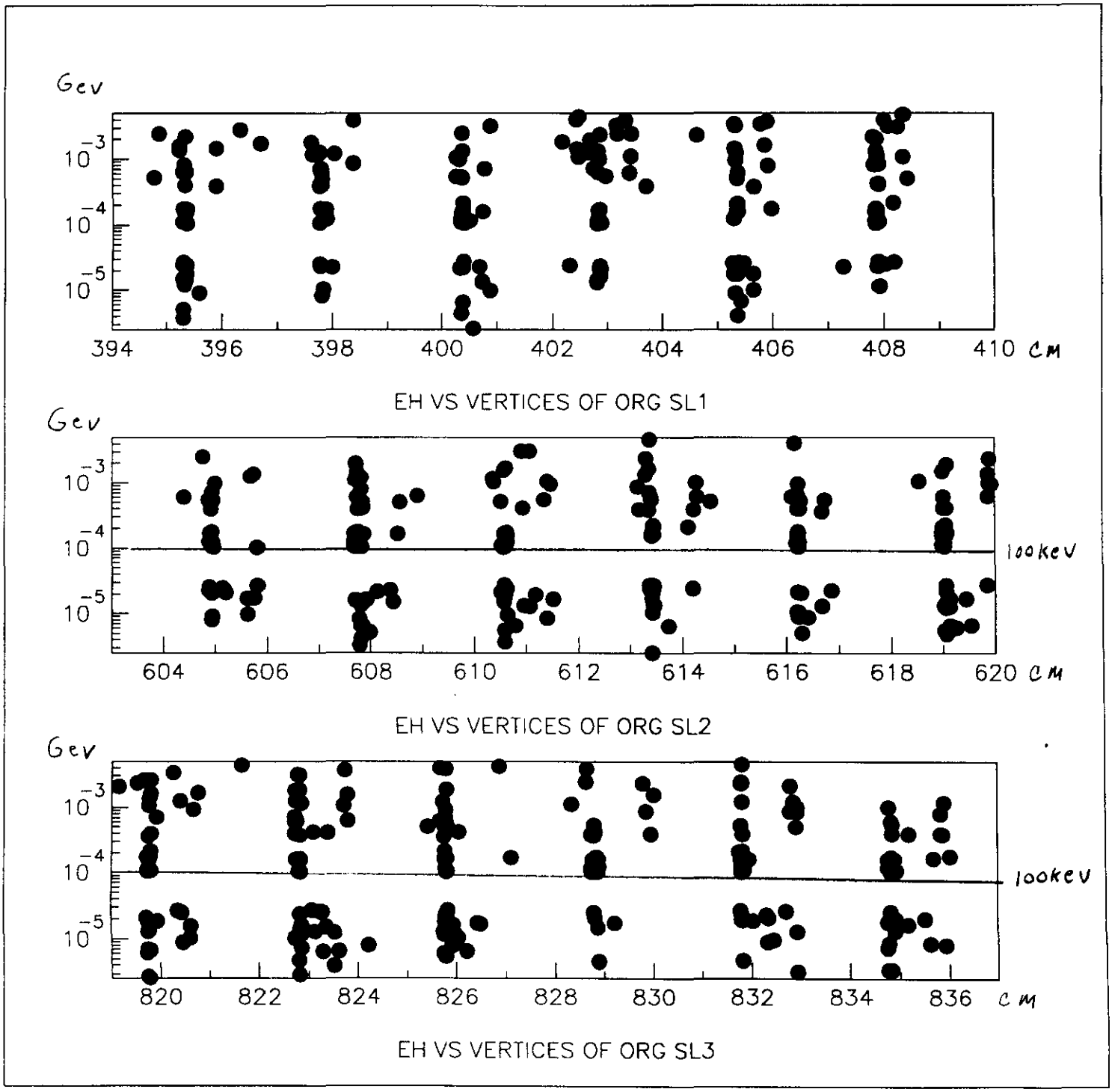

Figure 3a) Plots of energy vs radial origin outward of charged background through each of the superlayers for 500 1 TeV muon events at $\theta = 60^0$ and $\phi = 3^0$. Note that most of the background hits produced in the gas are low energy charged particles while most of the higher energy background are produce in or near the G10/Cu walls of the chambers.

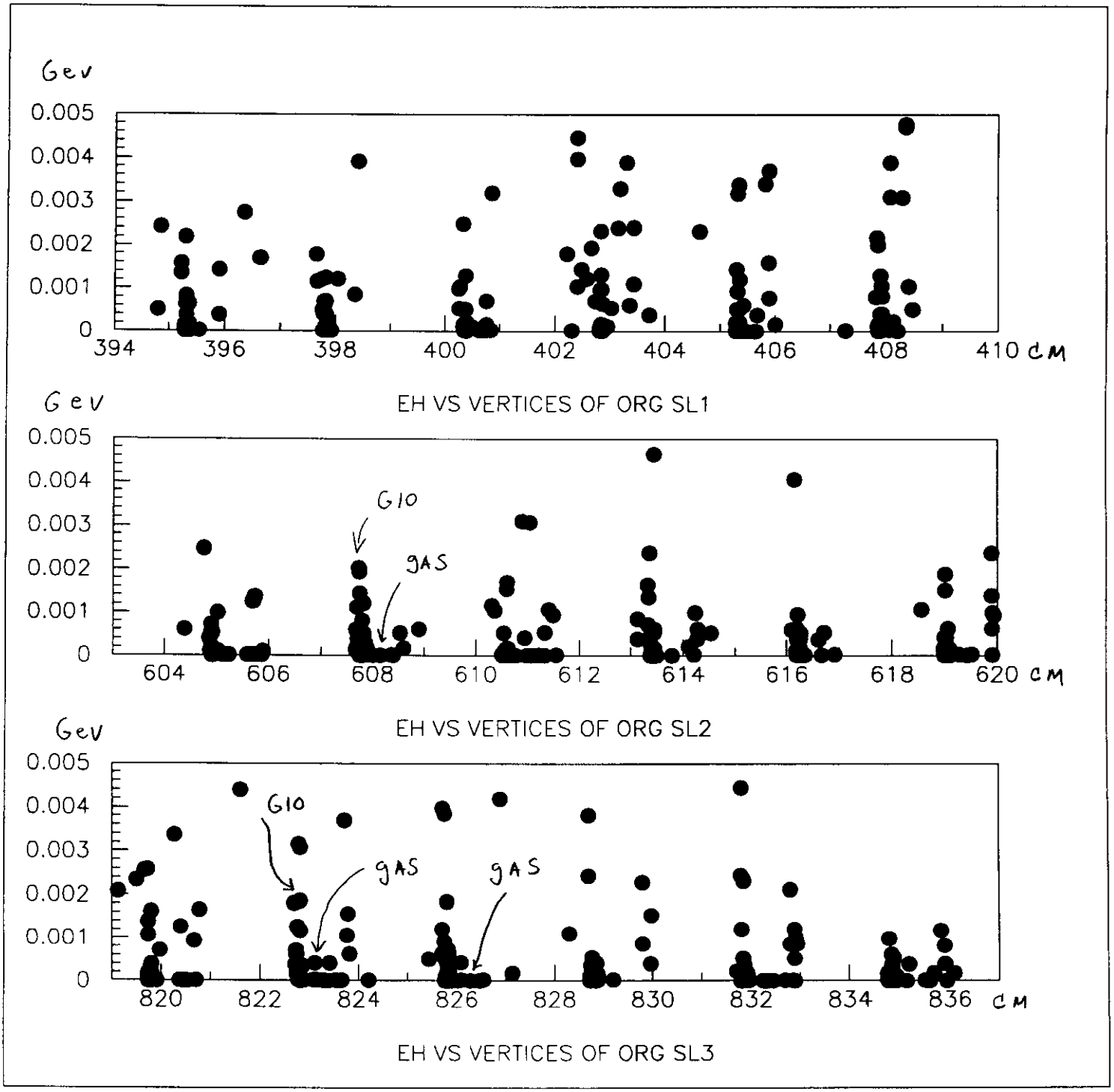

Figure 3b) Without a log scale on the energy one clearly sees the the origin of the low energy charged background component in the gas.

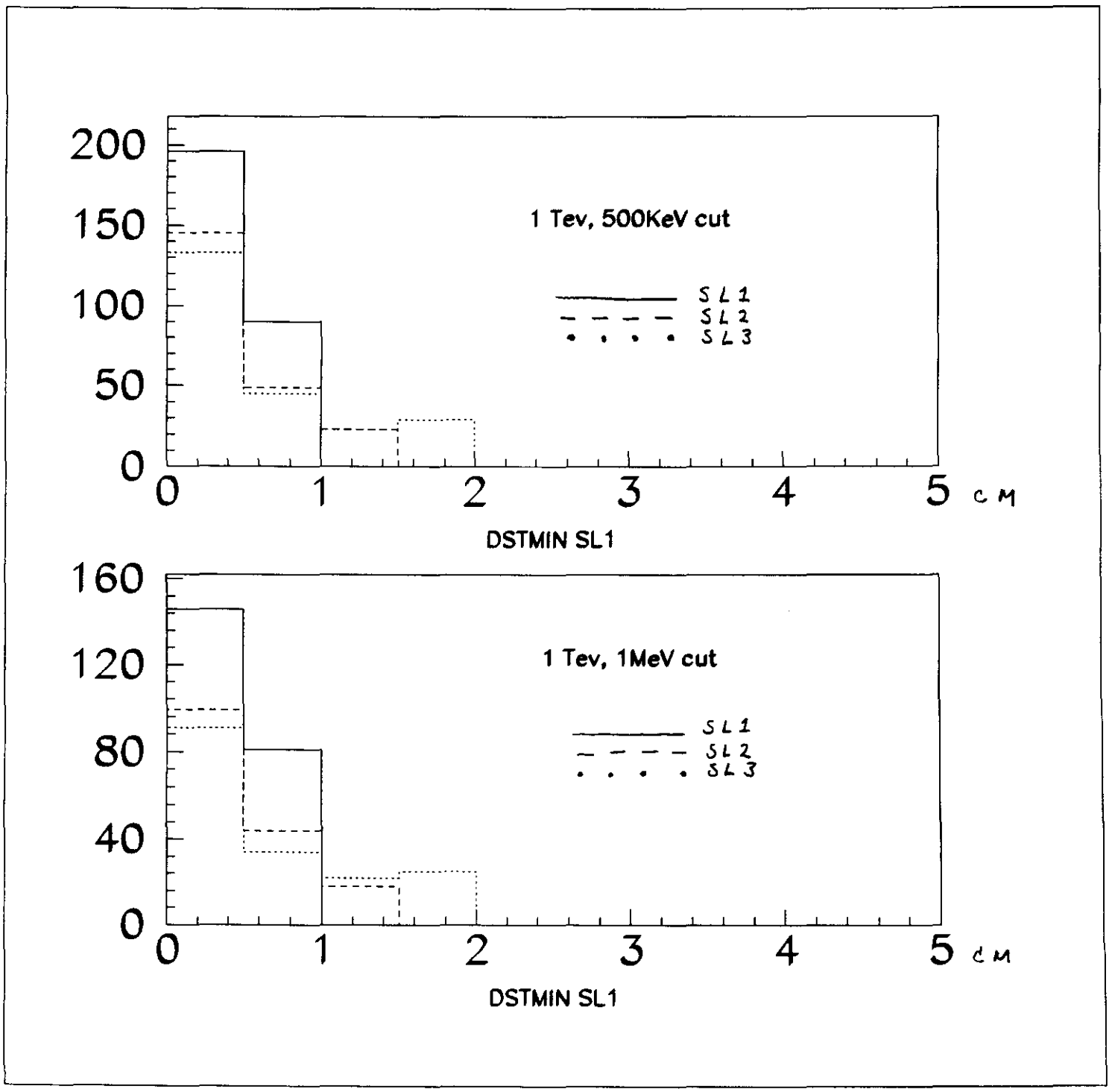

Figure 4) This figure shows the effect of successive energy cuts on the proximity distribution of charged background. Notice the major effect is in reducing the population of the first bin while the background farther away is much less effected. This demonstates that the close, soft correlated background is mostly in the gas. This figure should be compared to figure 2a.

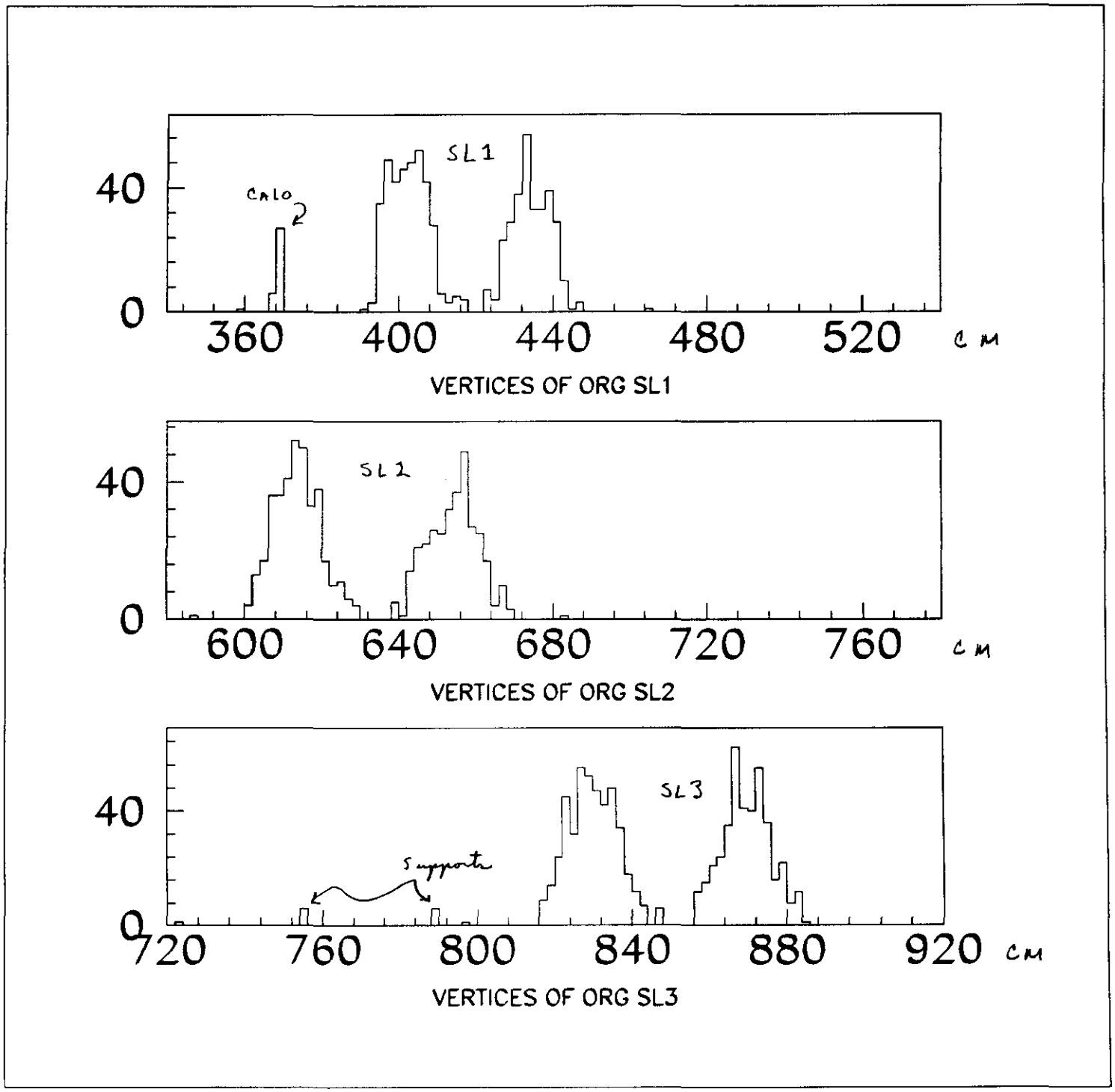

Figure 5a) These plots show the radial distribution of origins of charged background for the 1 TeV P_t muon sample, for each of the three superlayers in the barrel. Note the contribution by the calorimeter and structures.

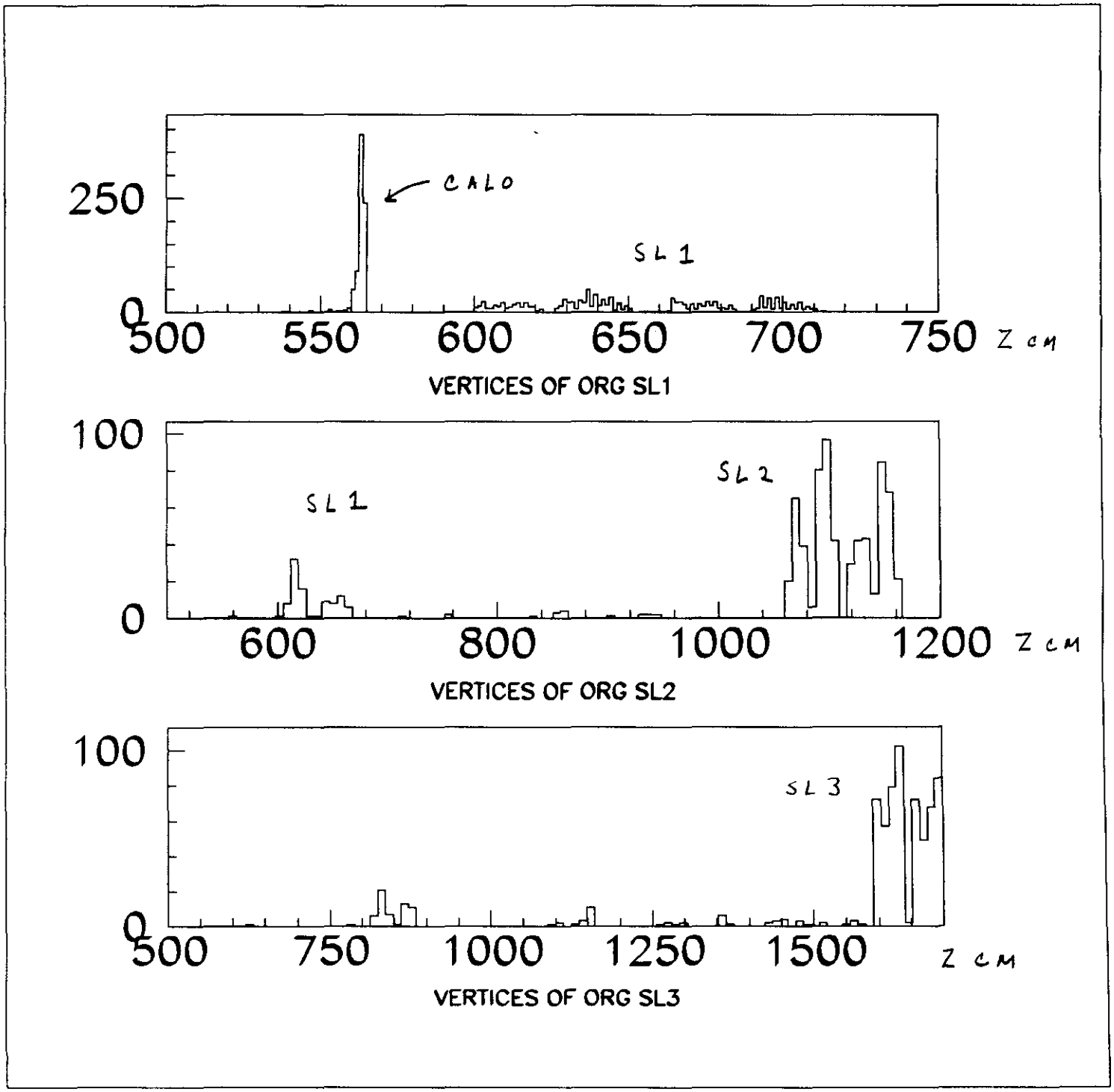

Figure 5b) These plots show the distribution, as a function of the "z" coordinate, of charged background in the endcap for the 1 TeV P_t sample. Notice the tremendous contibution to the background on the first superlayer made by the calorimeter.

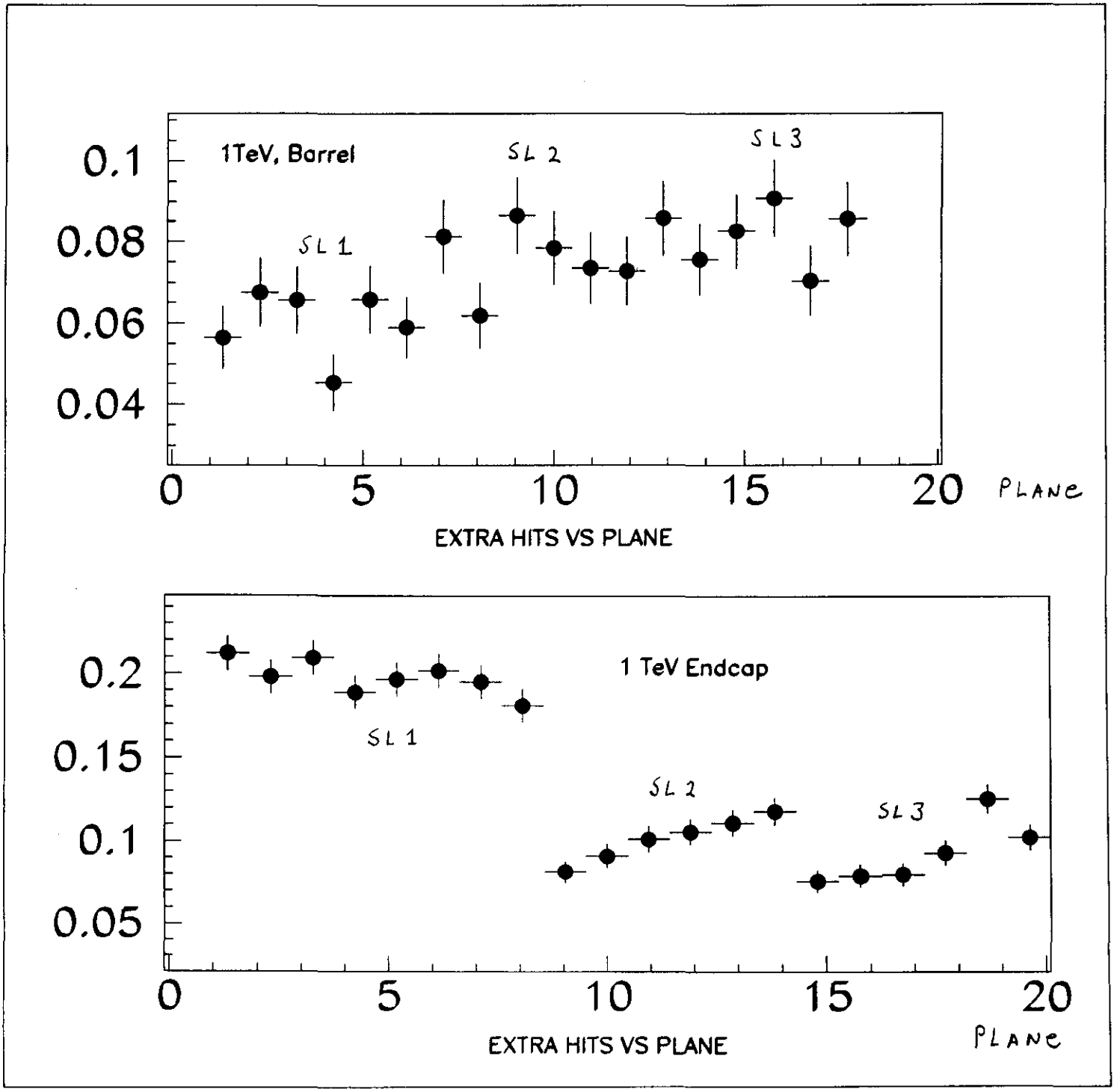

Figure 6) Occupancy of charged background within the "standard interval", as defined in the text, as a function of chamber in the barrel and endcap.

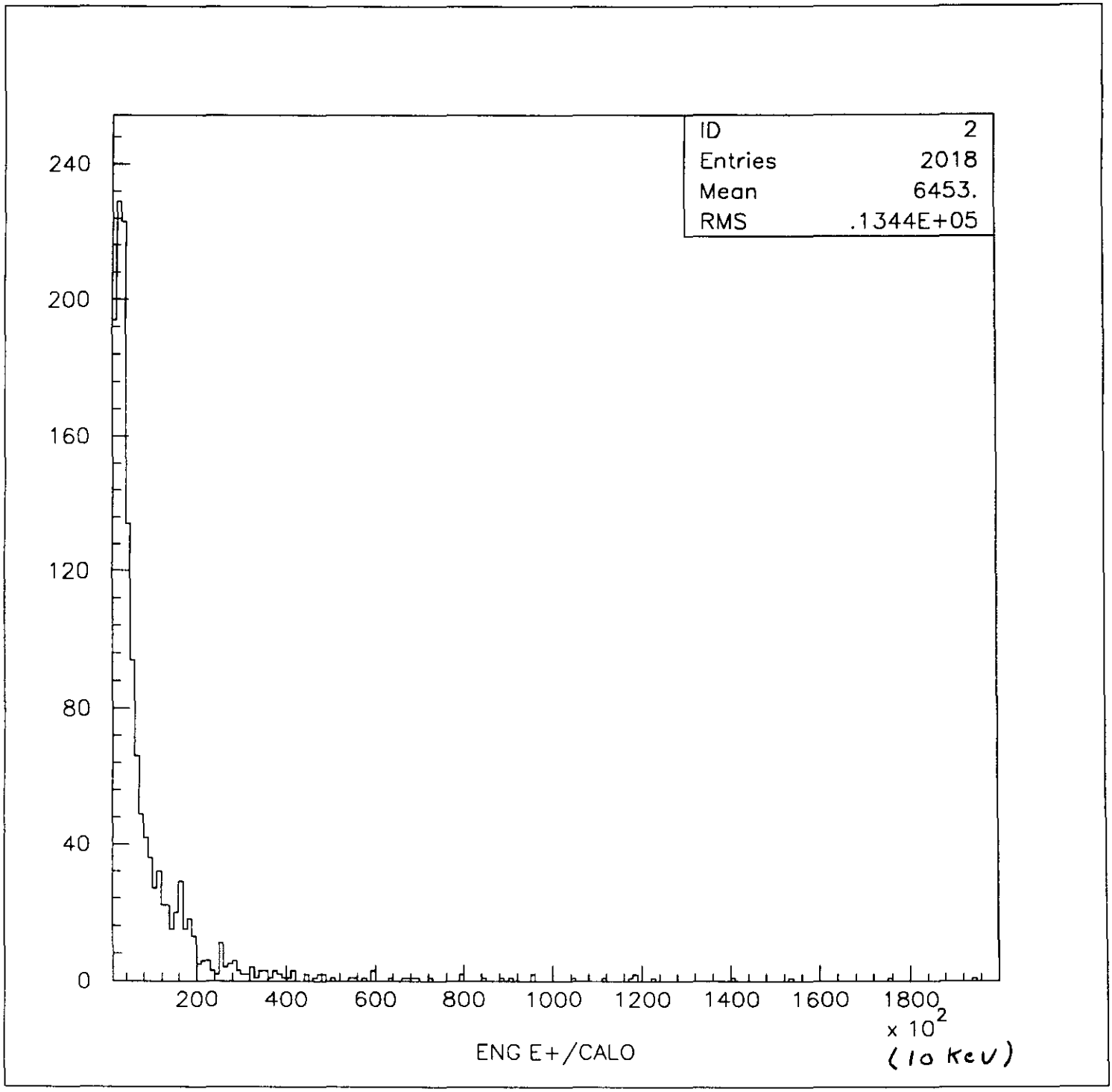

Figure 7a) Energy distribution of e^+ emerging from the calorimeter in the barrel. These are positrons correlated to 1 TeV muons, as is seen in the plot the average energy is $\sim 65 MeV$.

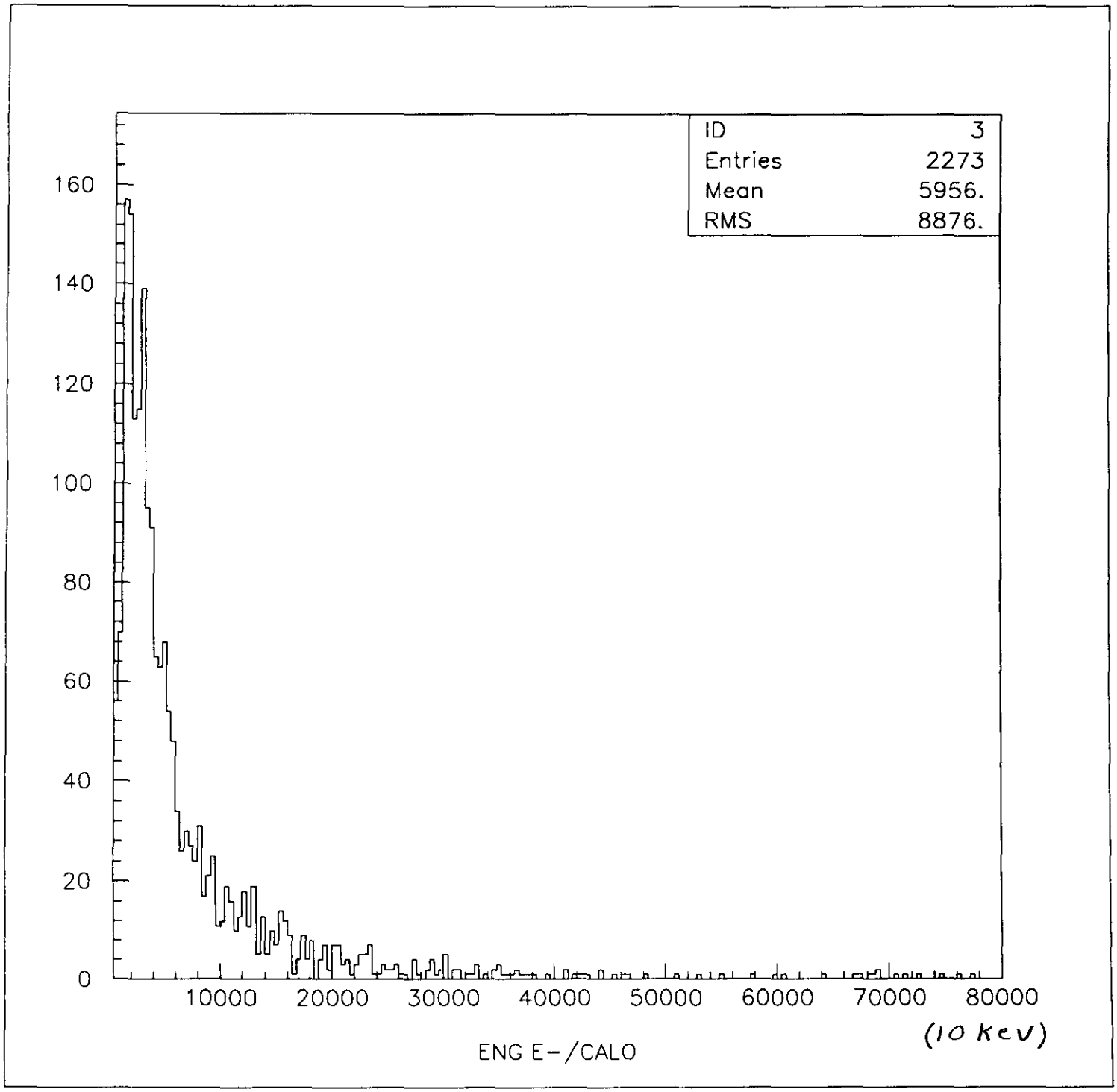

Figure 7b) Energy distribution of e^- emerging from the calorimeter in the barrel. These are electrons correlated to 1 TeV muons, as is seen in the plot the average energy is $\sim 59 MeV$.

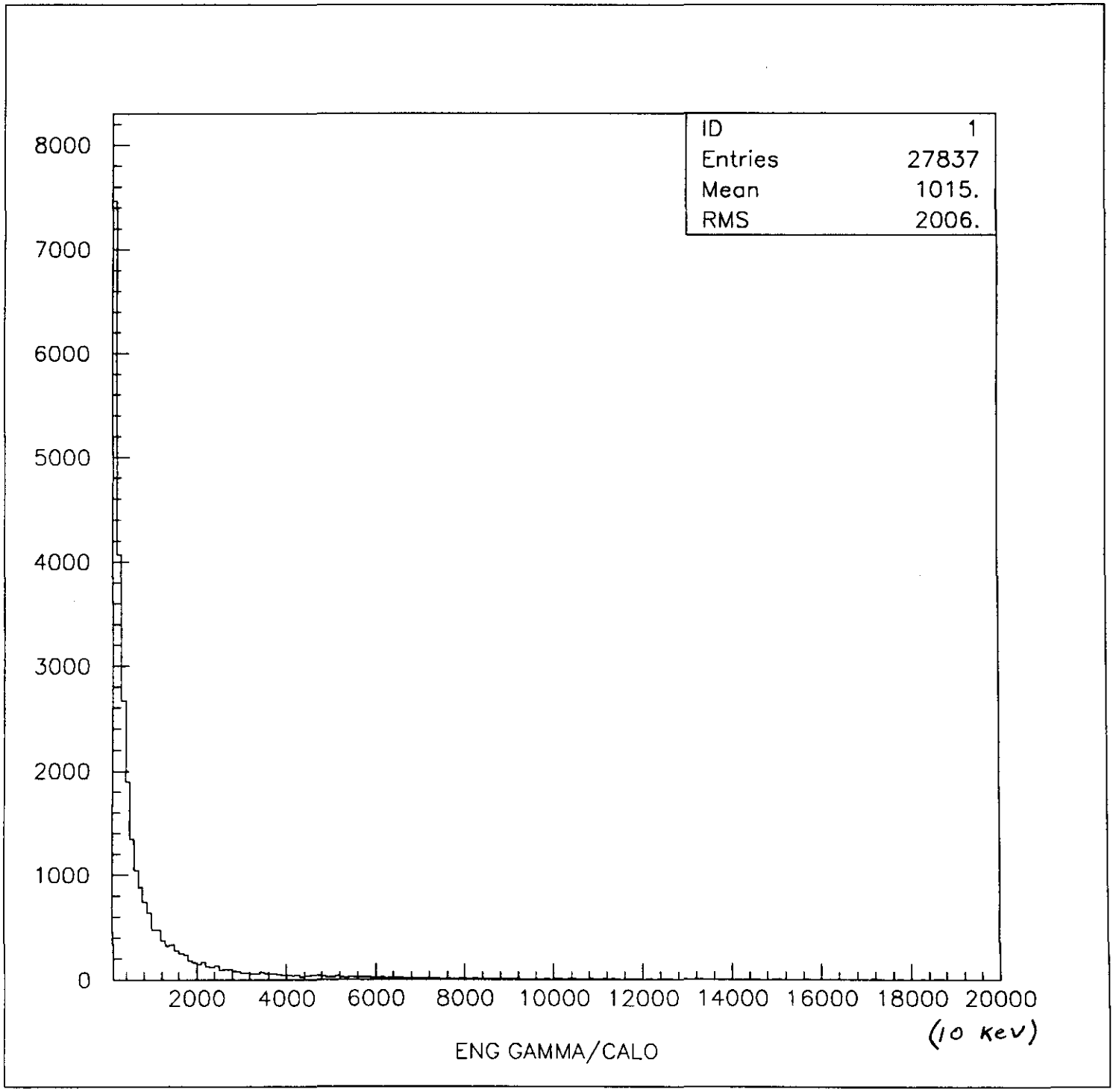

Figure 8a) Energy distribution of γ's emerging from the calorimeter in the barrel. These are γ's correlated to 1 TeV muons, as is seen in the plot the average energy is $\sim 10MeV$.

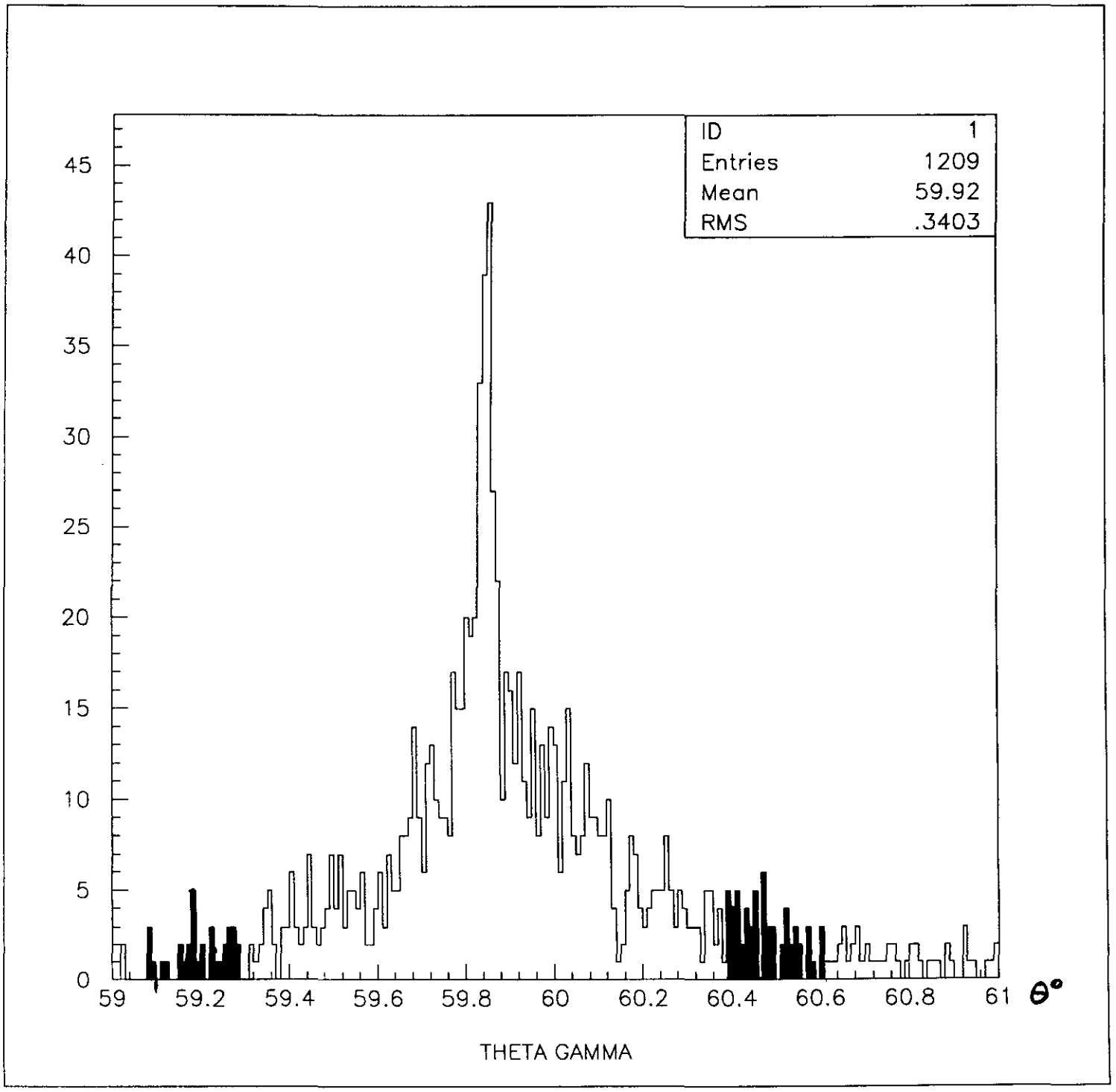

Figure 8b) Angular distribution of γ's emerging from the calorimeter in the barrel. These are γ's correlated to 1 TeV muons. The dark wings on either side of the peak is the increase in the number of γ's that can reach the standard interval on superlayer 2 as compared to superlayer 3.

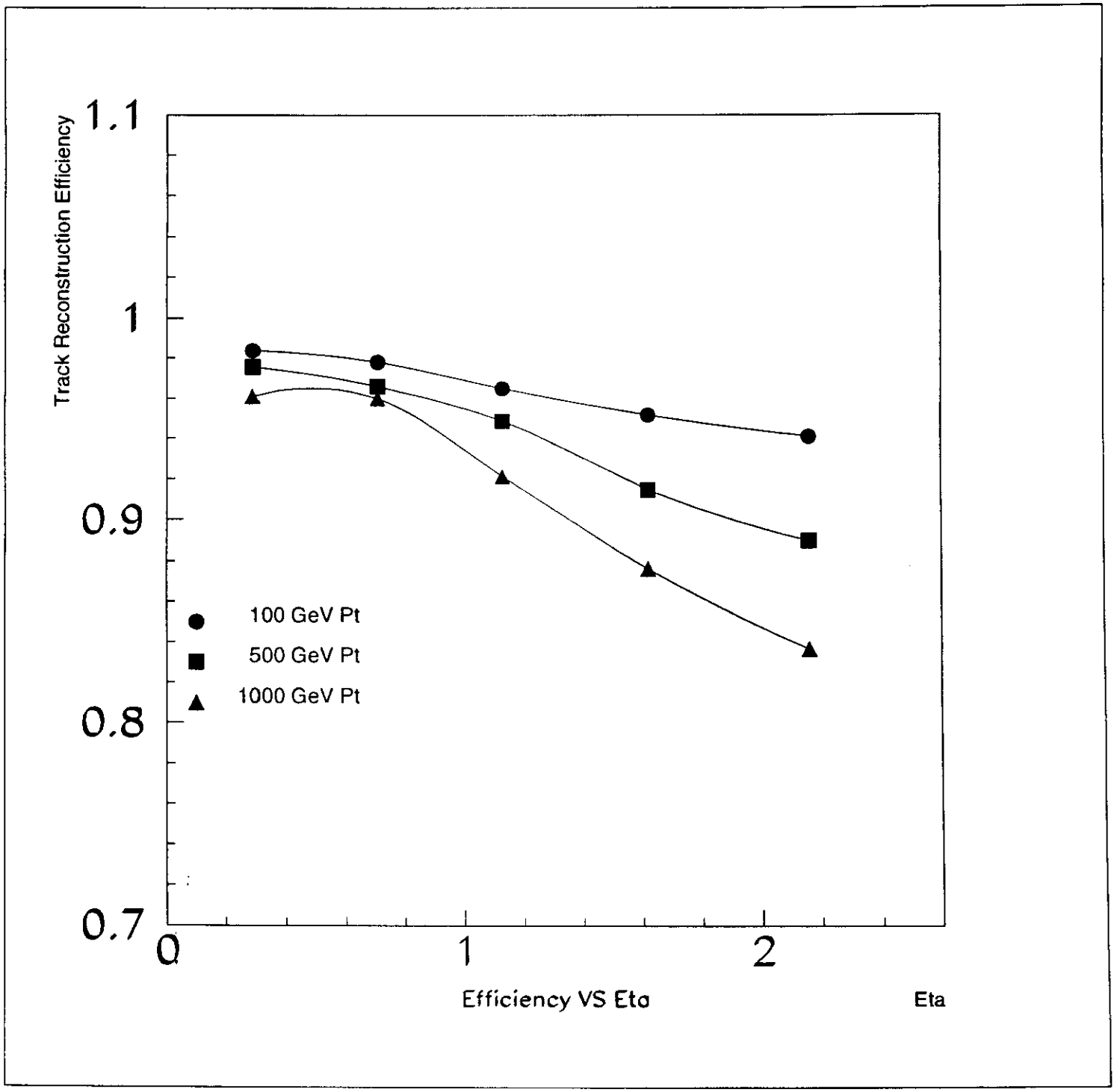

Figure 9) Track finding efficiency as a function of η using the "three good hits" method

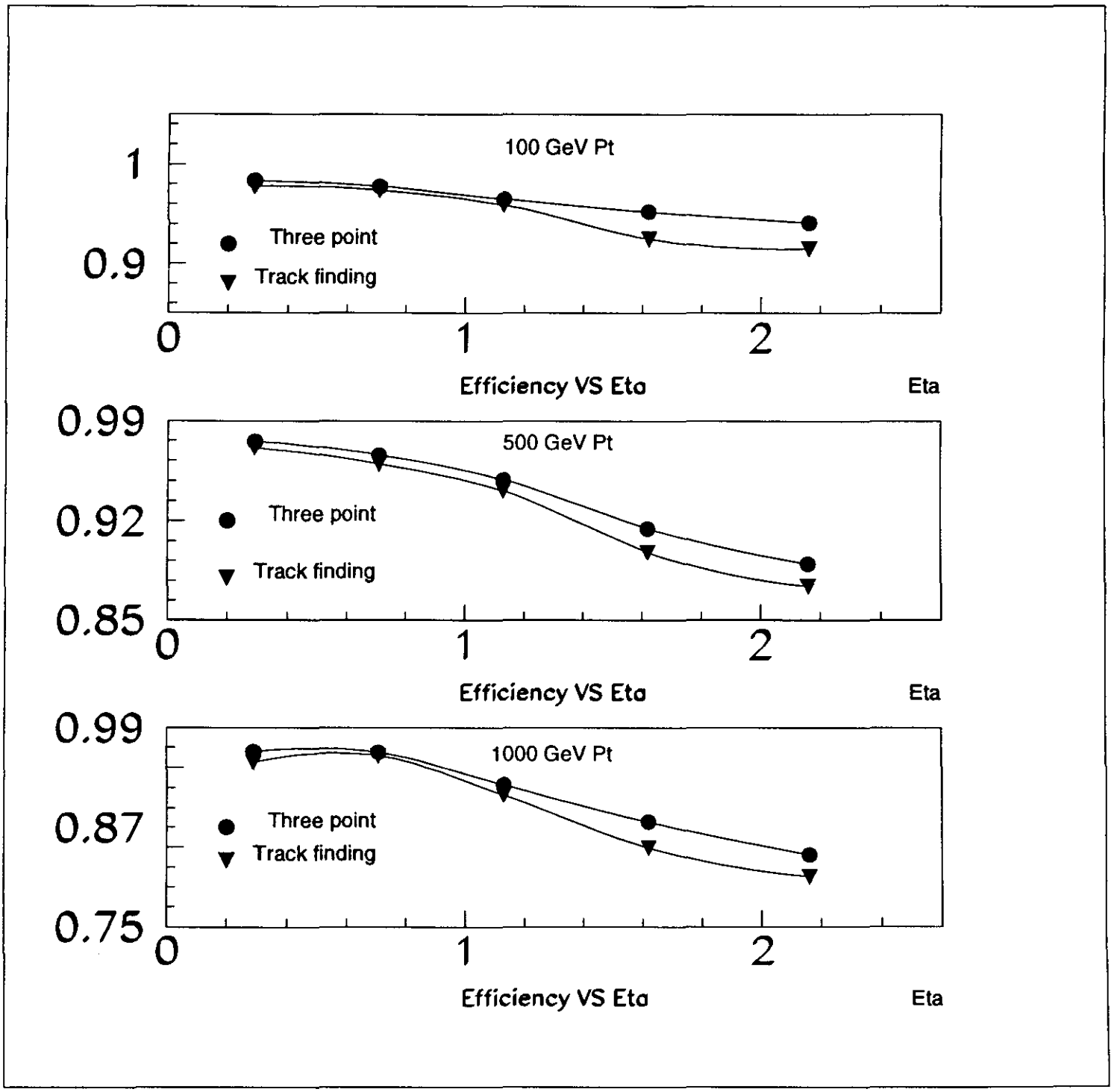

Figure 10) Comparison of the track finding efficiency using the "three good hits" method and the cluster search-merge algorithm discribed in the text. The comparison is made by using a preselected data set where three "good" hits had already been found, thus showing the inefficiency of the cluster algorithm. The cluster algorithm is shown to be very efficient .

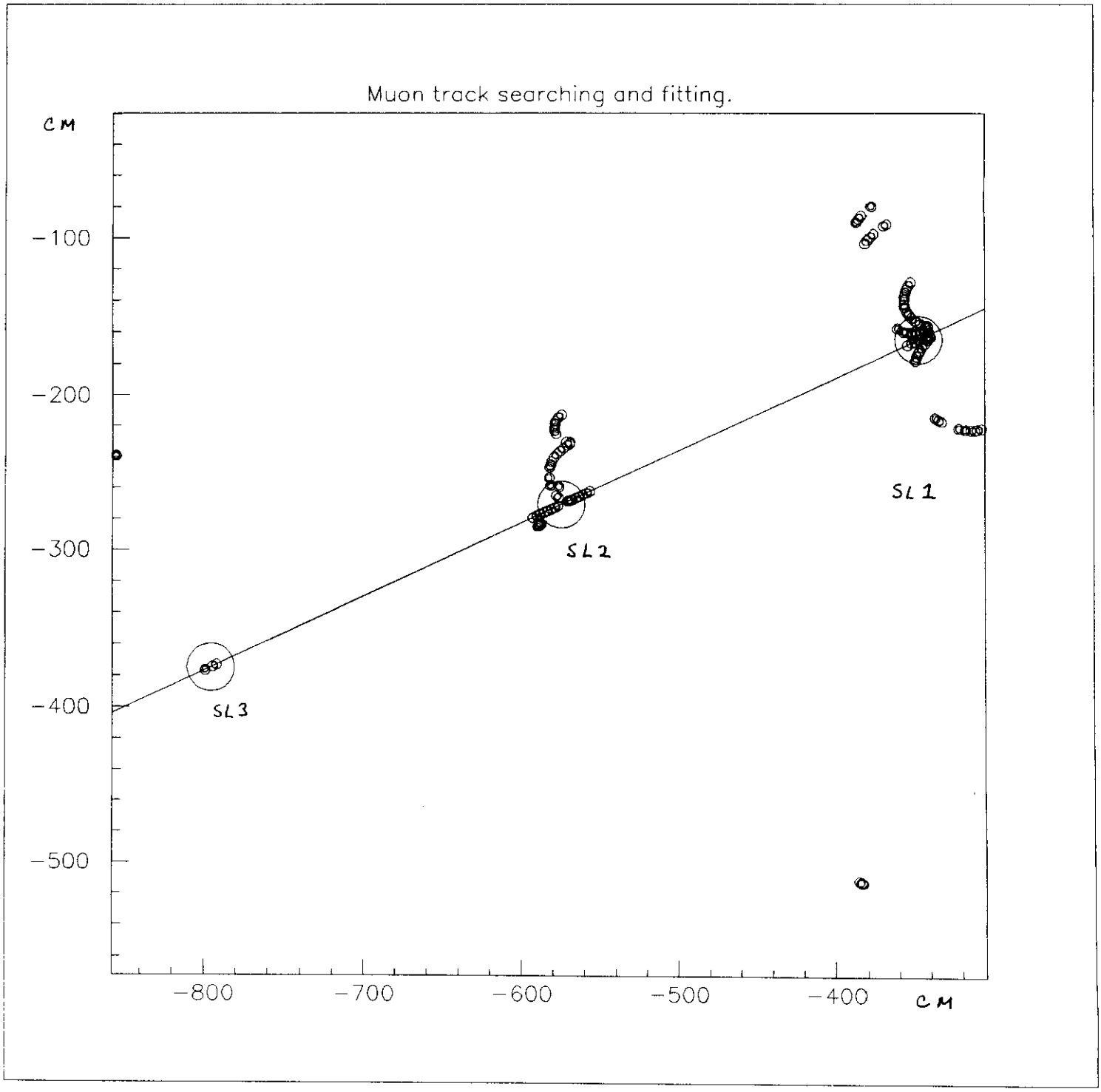

Figure 11) Track found using the cluster search-merge algorithm .

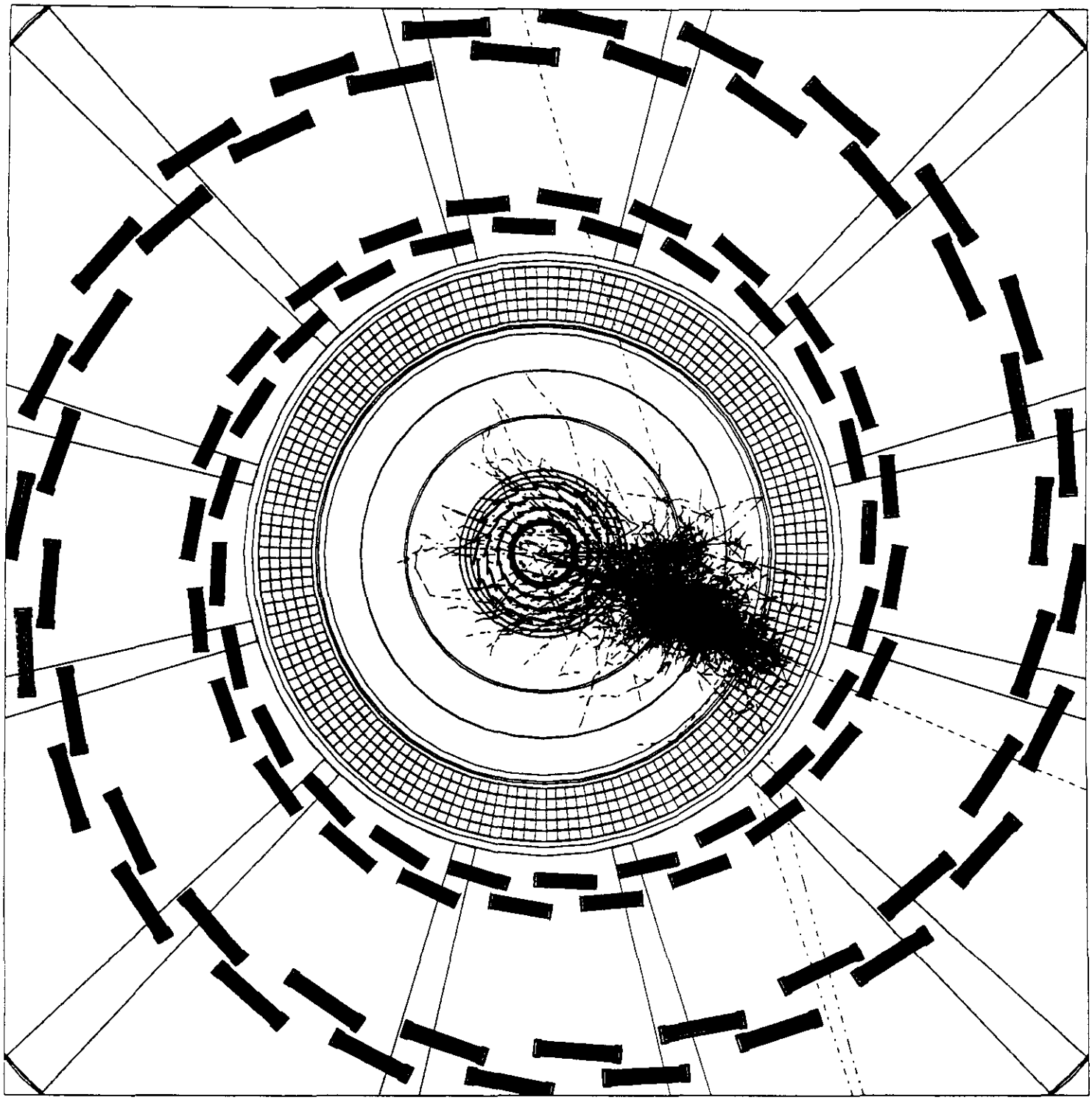

Figure 12a) 500 GeV μ (the dashed line), in the barrel, coming from the decay of a **b** quark coming from a $t\bar{t}$ event. All particles in a cone of $r = \sqrt{\Delta\eta^2 + \Delta\phi^2} < 1.0$ with $E \geq 3.0$ GeV are passed to the simulation .

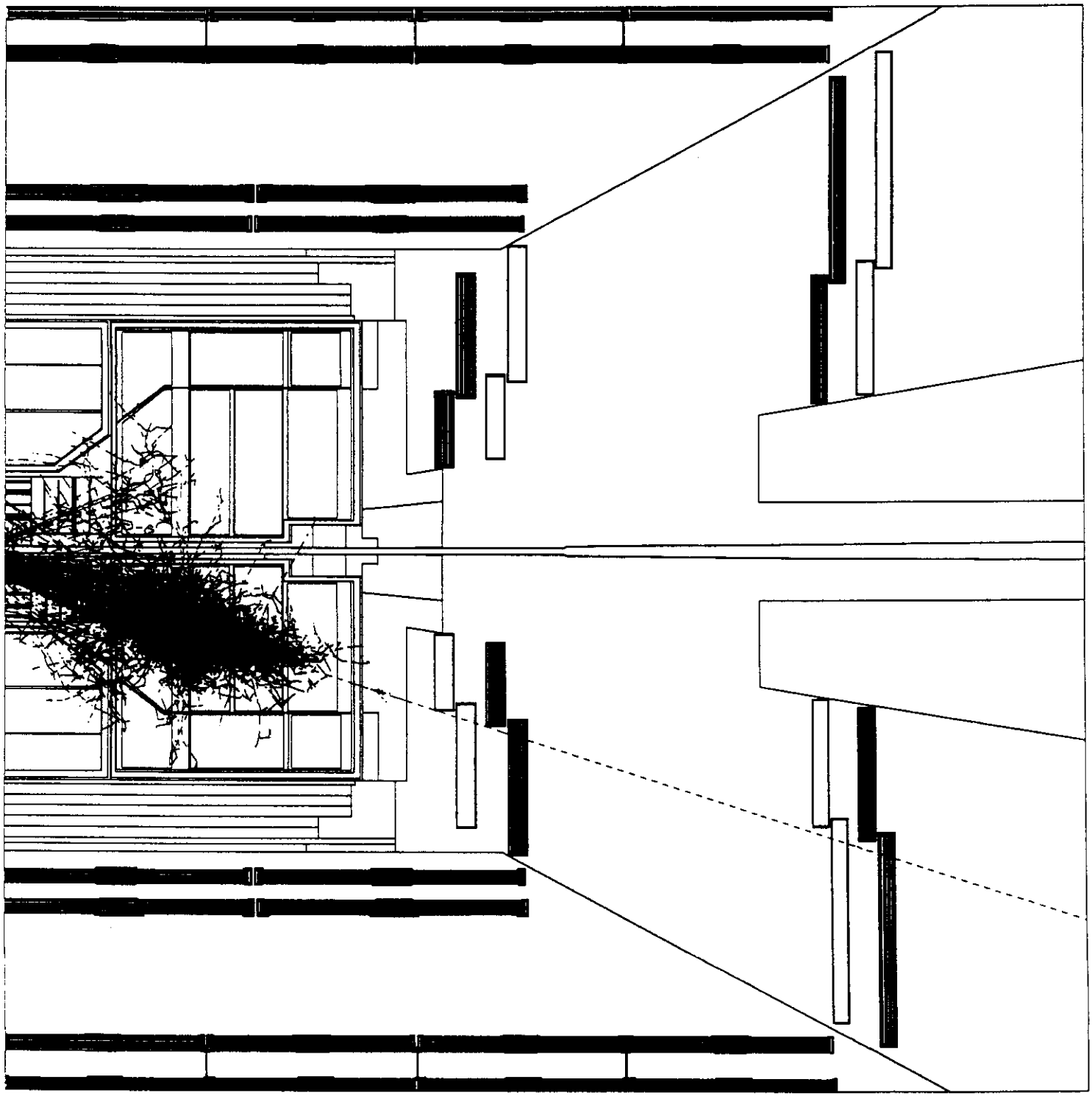

Figure 12b) 135 GeV μ (the dashed line), in the endcap, coming from the decay of a b quark coming from a $t\bar{t}$ event. All particles in a cone of $r = \sqrt{\Delta\eta^2 + \Delta\phi^2} < 1.0$ with $E \geq 3.0$ GeV are passed to the simulation .

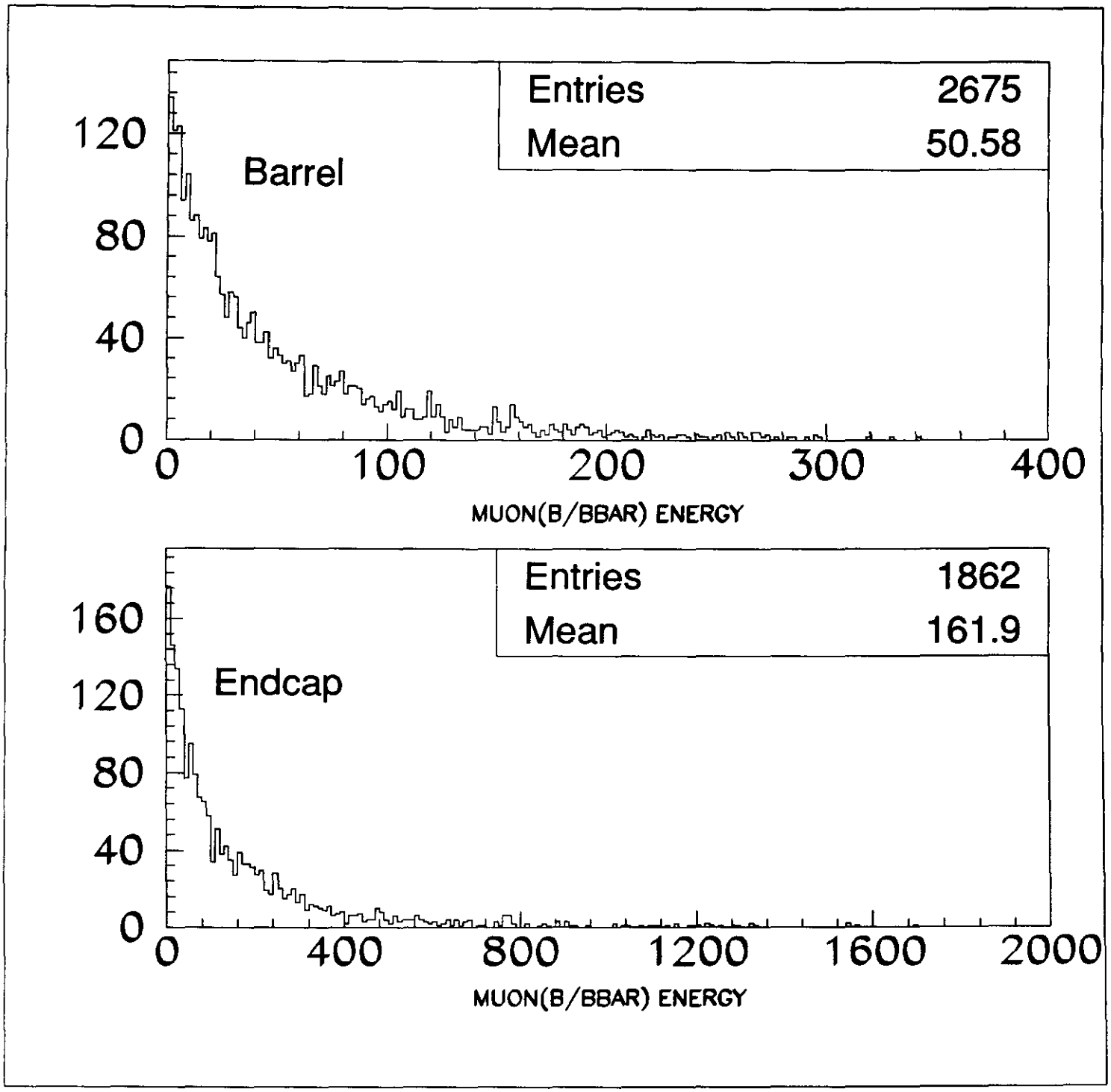

Figure 12c) Energy distributions in the barrel and endcap of μ's from the decay of a b quark, coming from $t\bar{t}$ events.

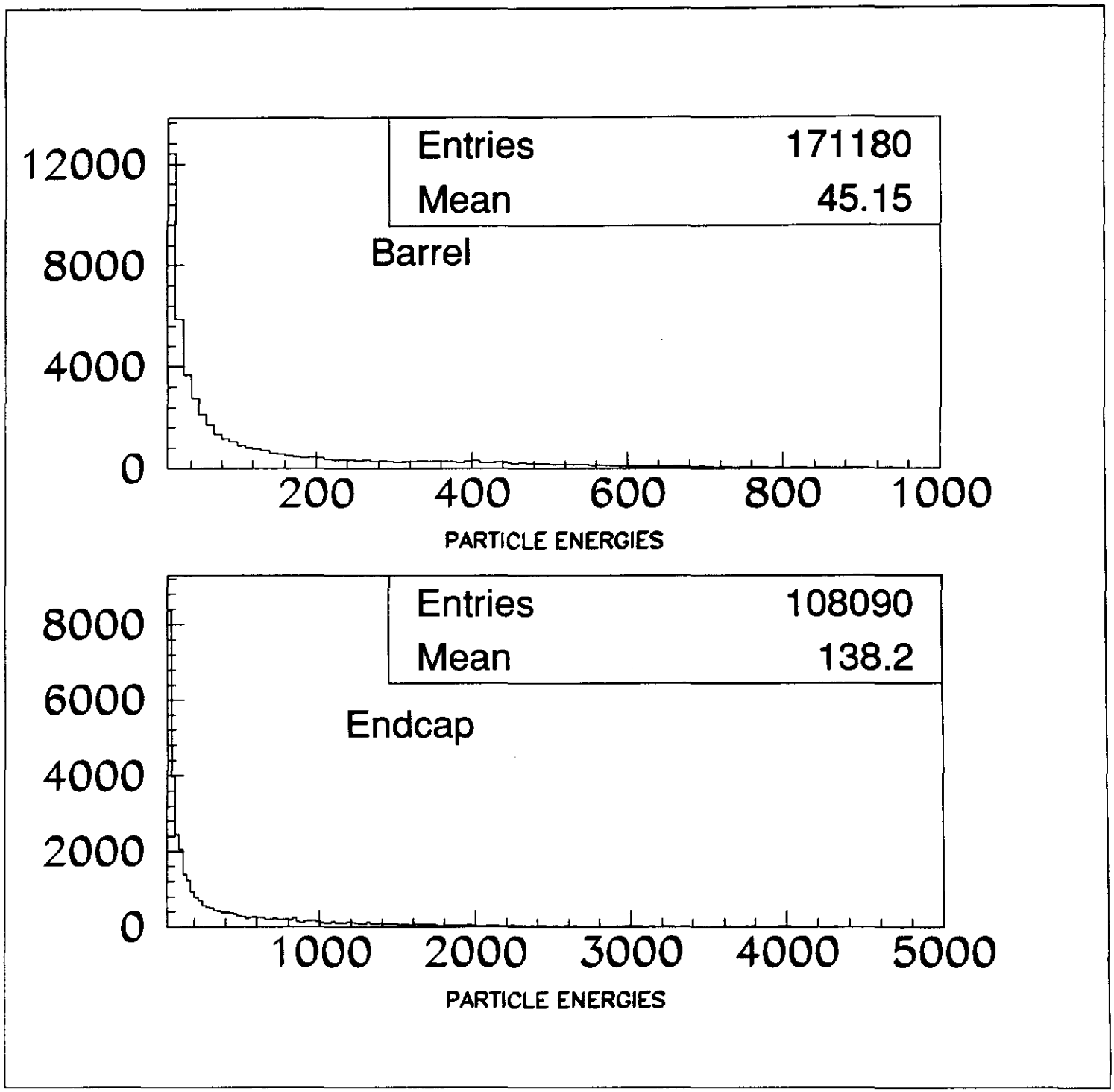

Figure 12d) Energy distributions of particles contained in a cone of $r = \sqrt{\Delta\eta^2 + \Delta\phi^2} < 1.0$ around μ's coming from b quarks, coming from $t\bar{t}$ events.

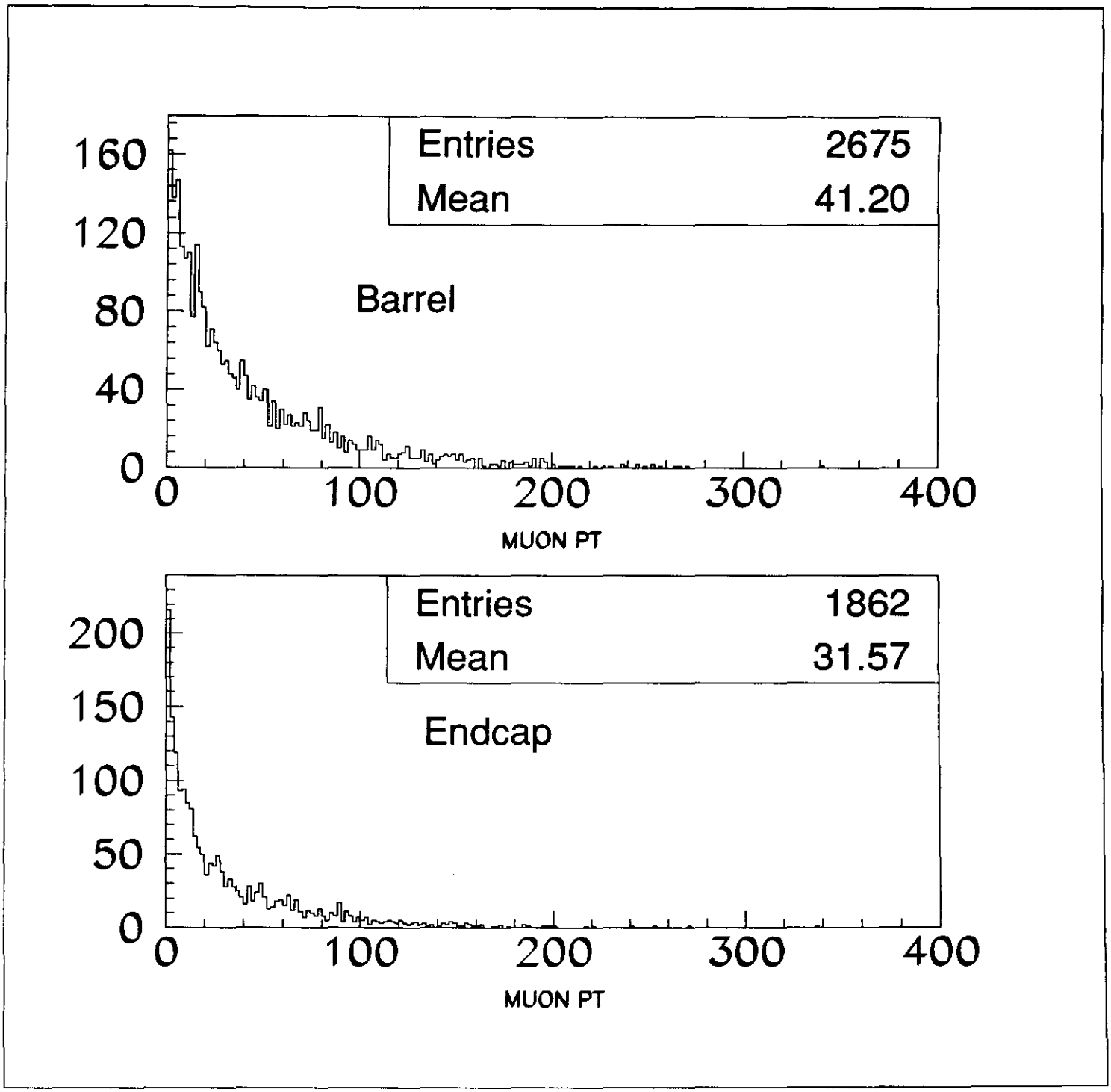

Figure 12e) P_t distributions of μ's coming from b quark decay, coming from $t\bar{t}$ events in the barrel and endcap.

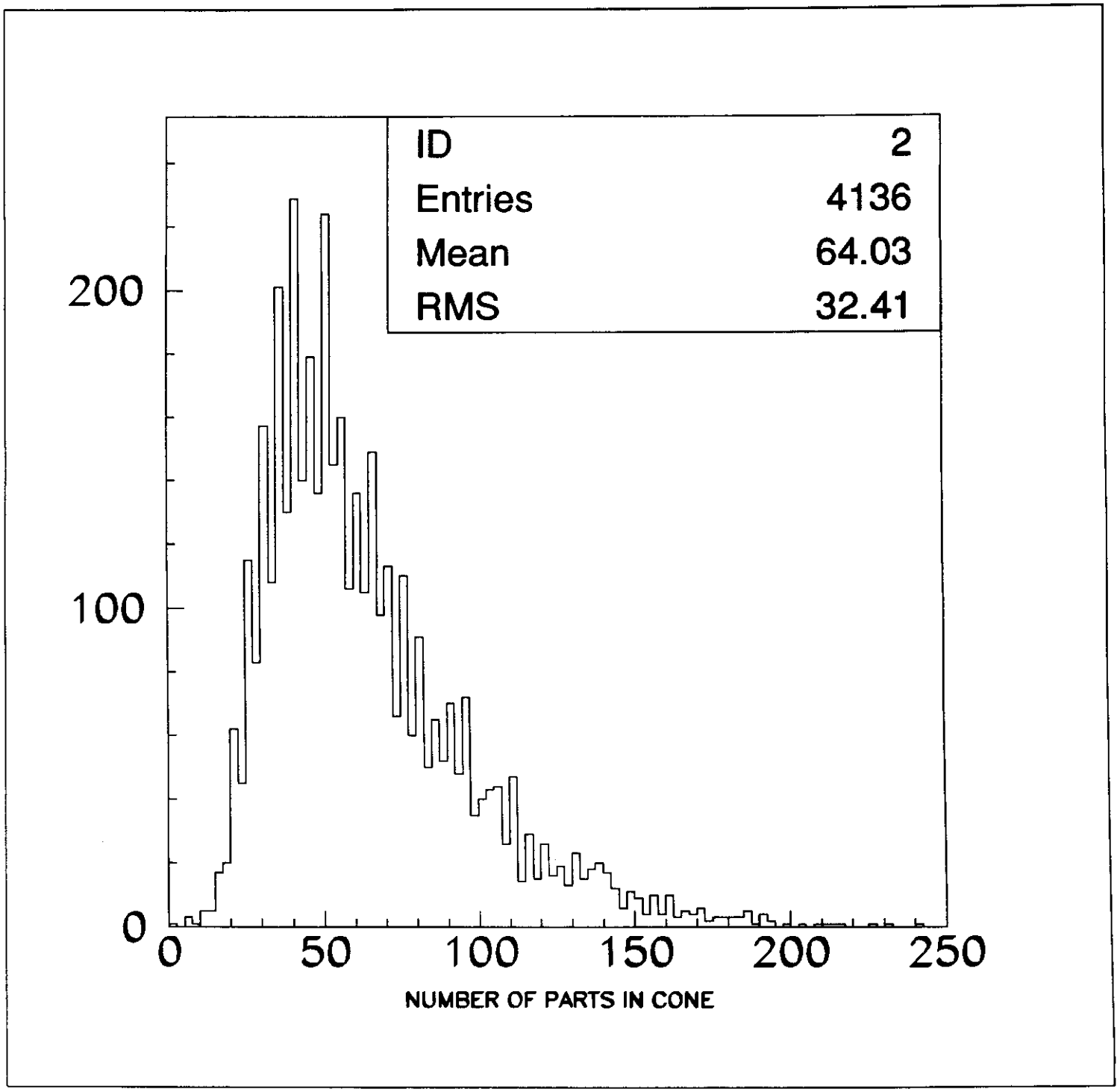

Figure 12f) Number of particles in a cone $r = \sqrt{\Delta\eta^2 + \Delta\phi^2}$ around μ's coming from the decay of **b** quarks.

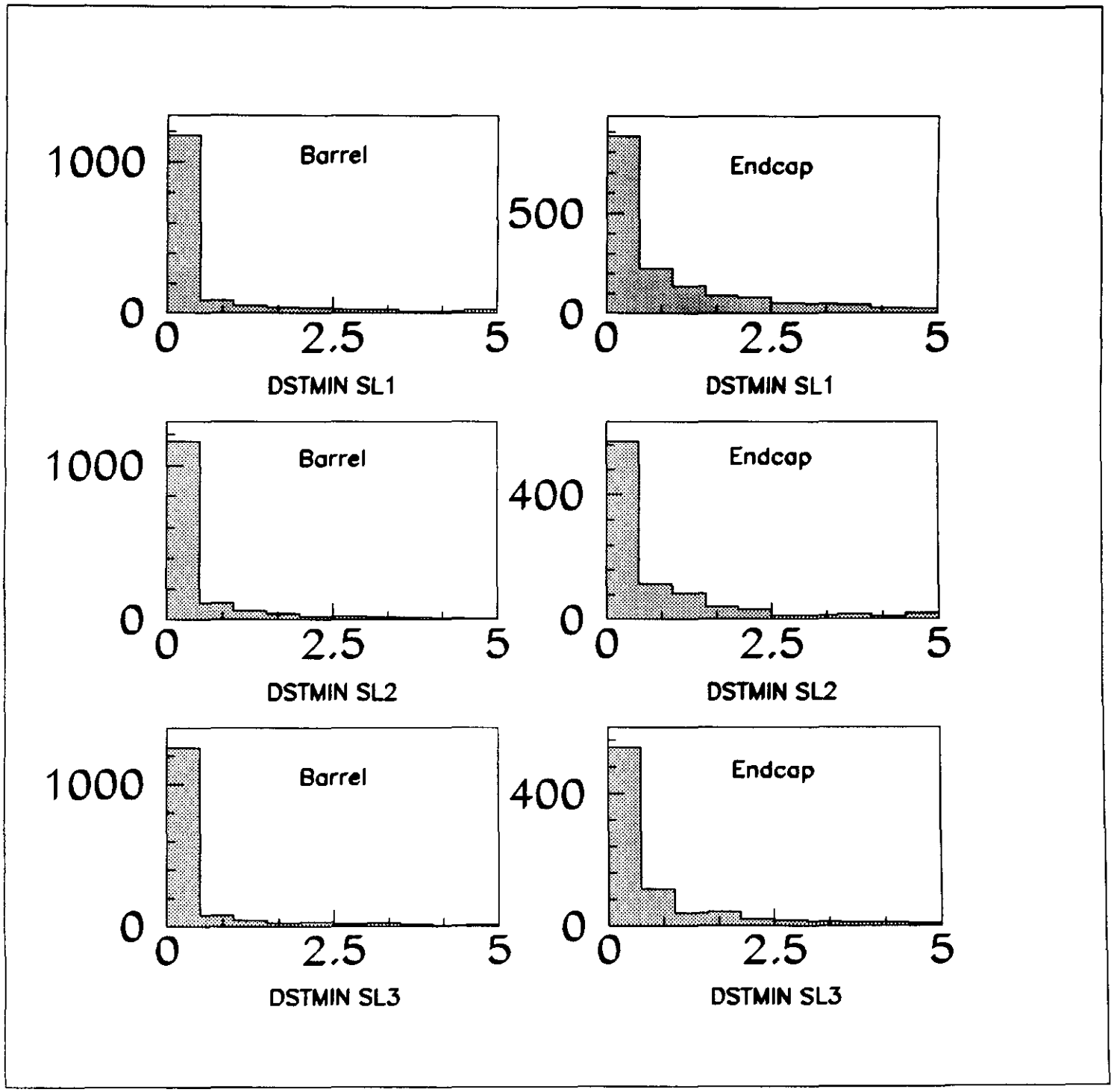

Figure 13) These plots show the distribution of secondary charged hits around the muon, for muons coming from **b** quarks that are the decay products of **t** quarks in $t\bar{t}$ events. Shown are the distributions in both the barrel and endcap muon systems for each of the three superlayers.

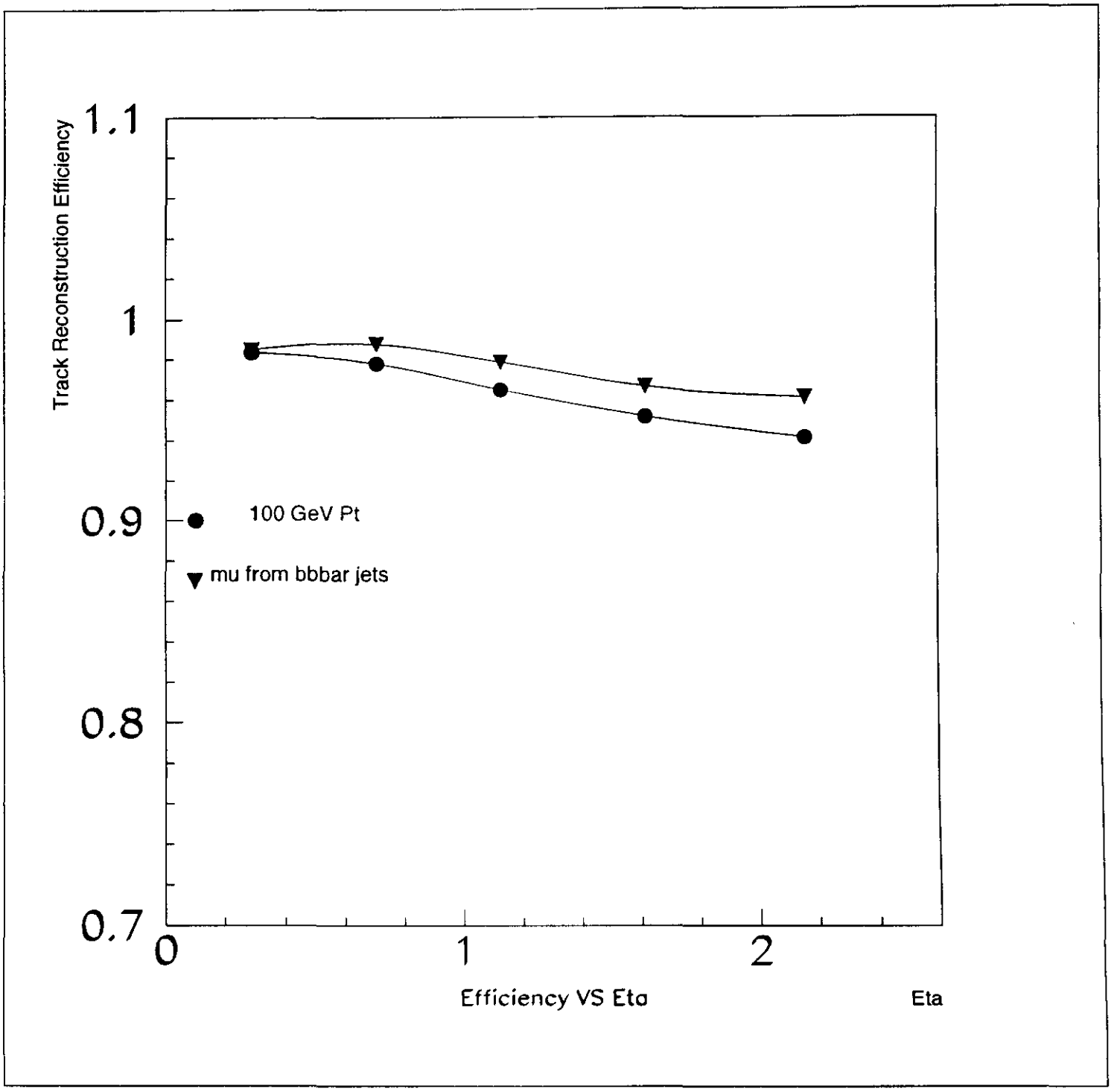

Figure 14) The efficiency, computed via the "three good hit" method, for finding muon tracks coming from b decay in $t\bar{t}$ events compared to that of the isolated 100 GeV P_t muon sample .

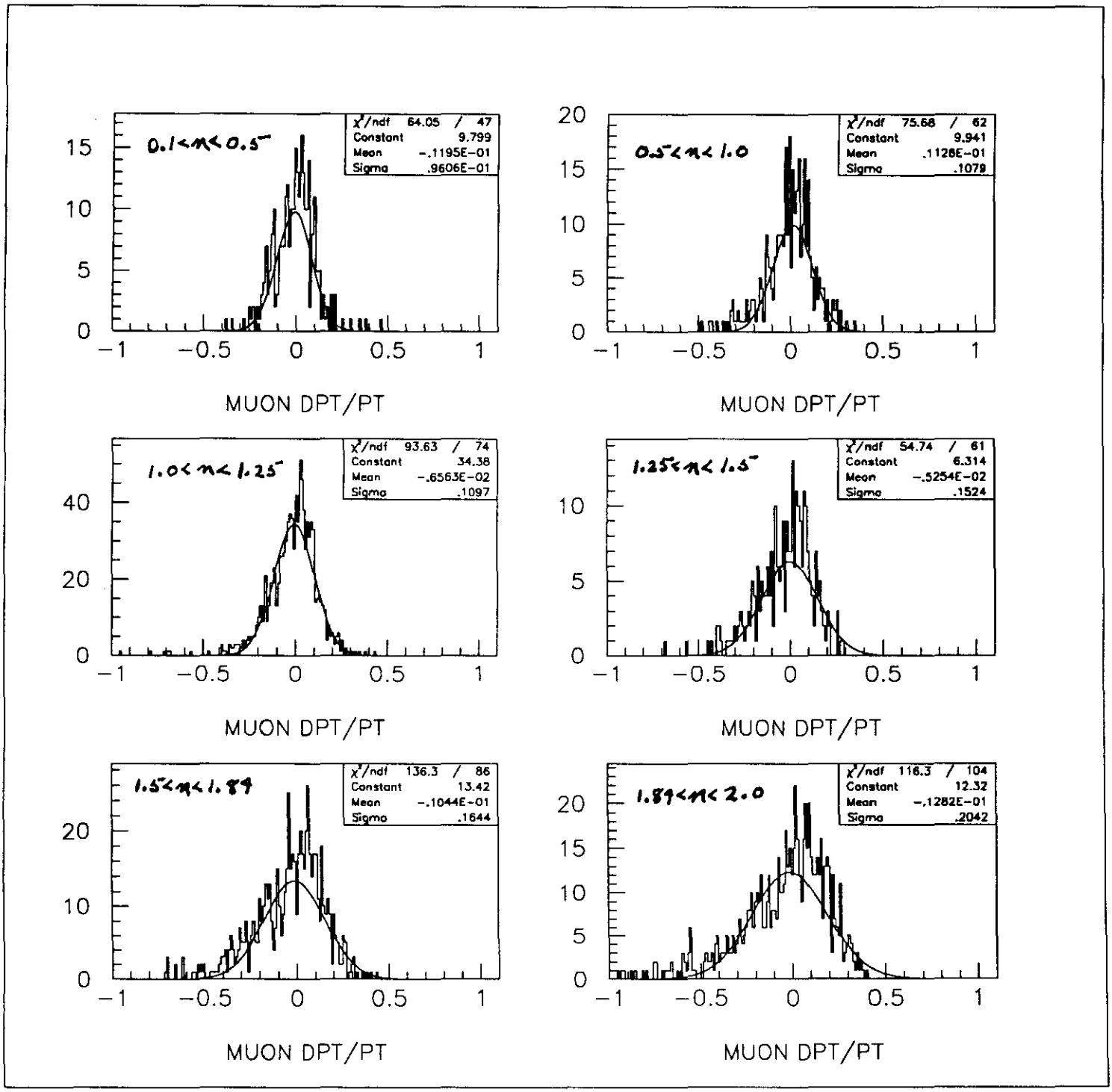

Figure 15a) Resolution distributions as a function of η for the isolated 1 TeV P_t muon sample, including all correlated backgrounds, computed by the Kalman Filter .

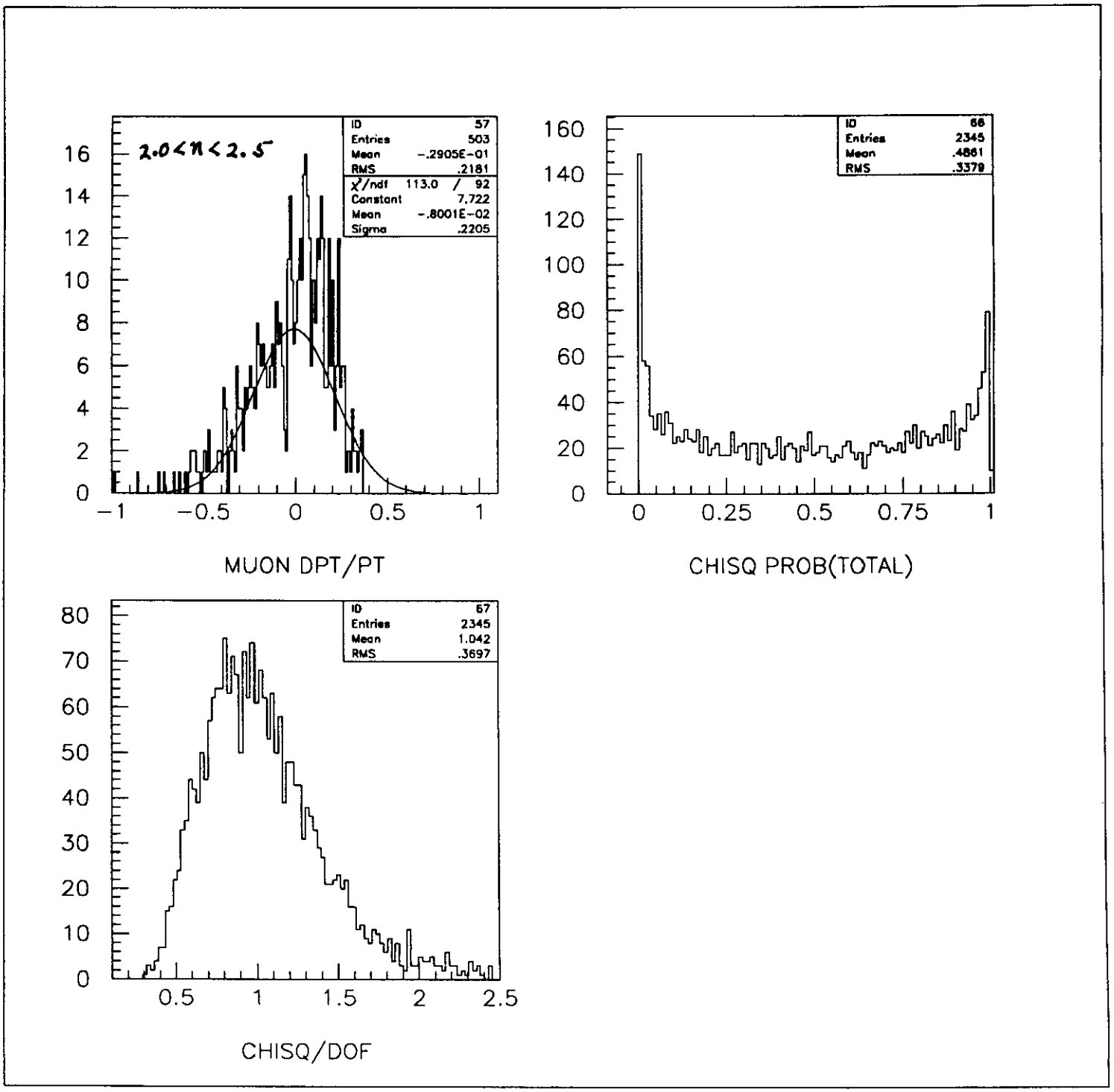

Figure 15b) Distributions of χ^2 probability and $\frac{\chi^2}{DOF}$ resulting from the Kalman Filter track fit for the 1 TeV muon sample with background .

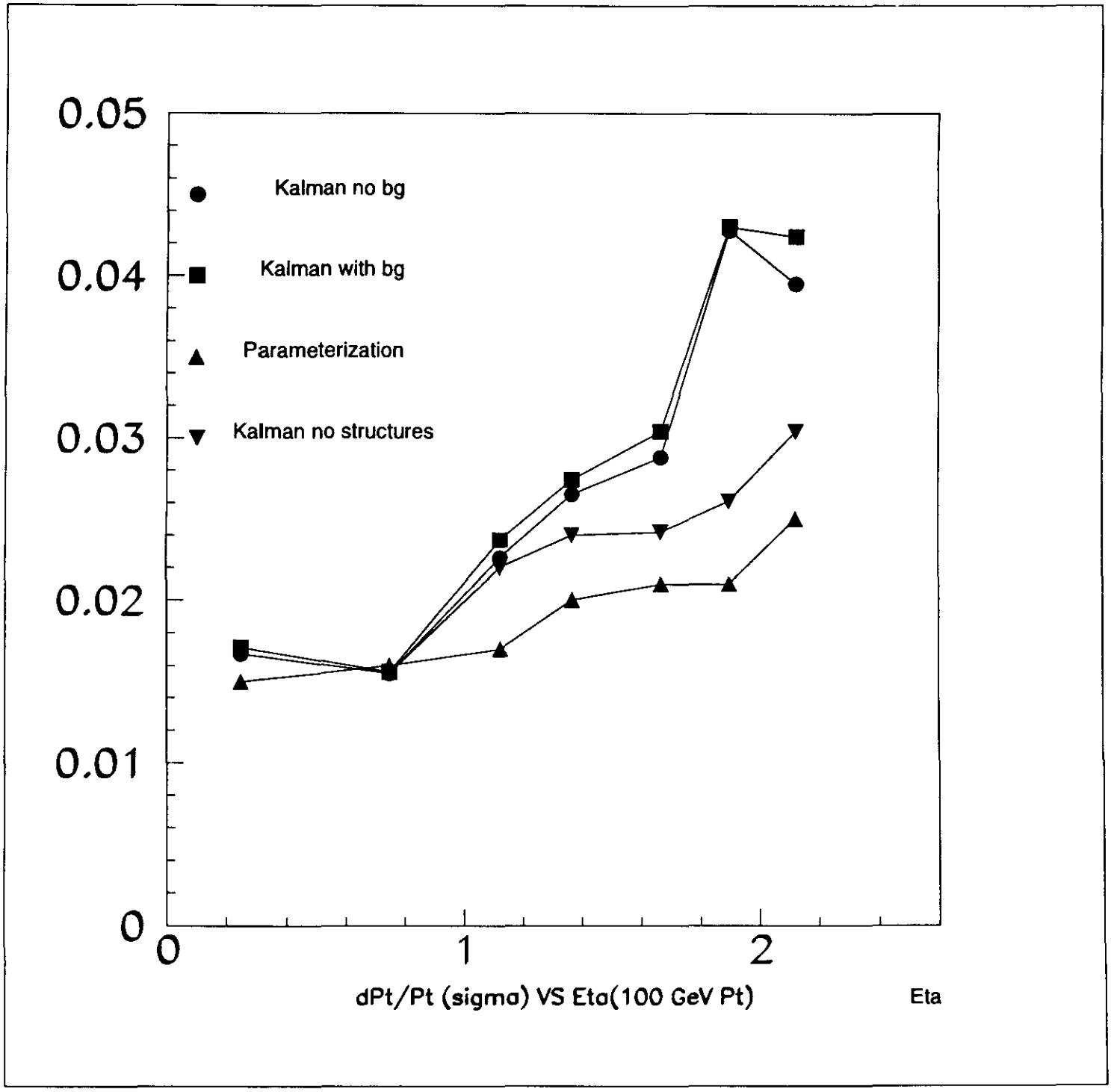

Figure 16) Track resolution plot as a function of η for the 100 GeV P_t muon sample using the Kalman Filter .

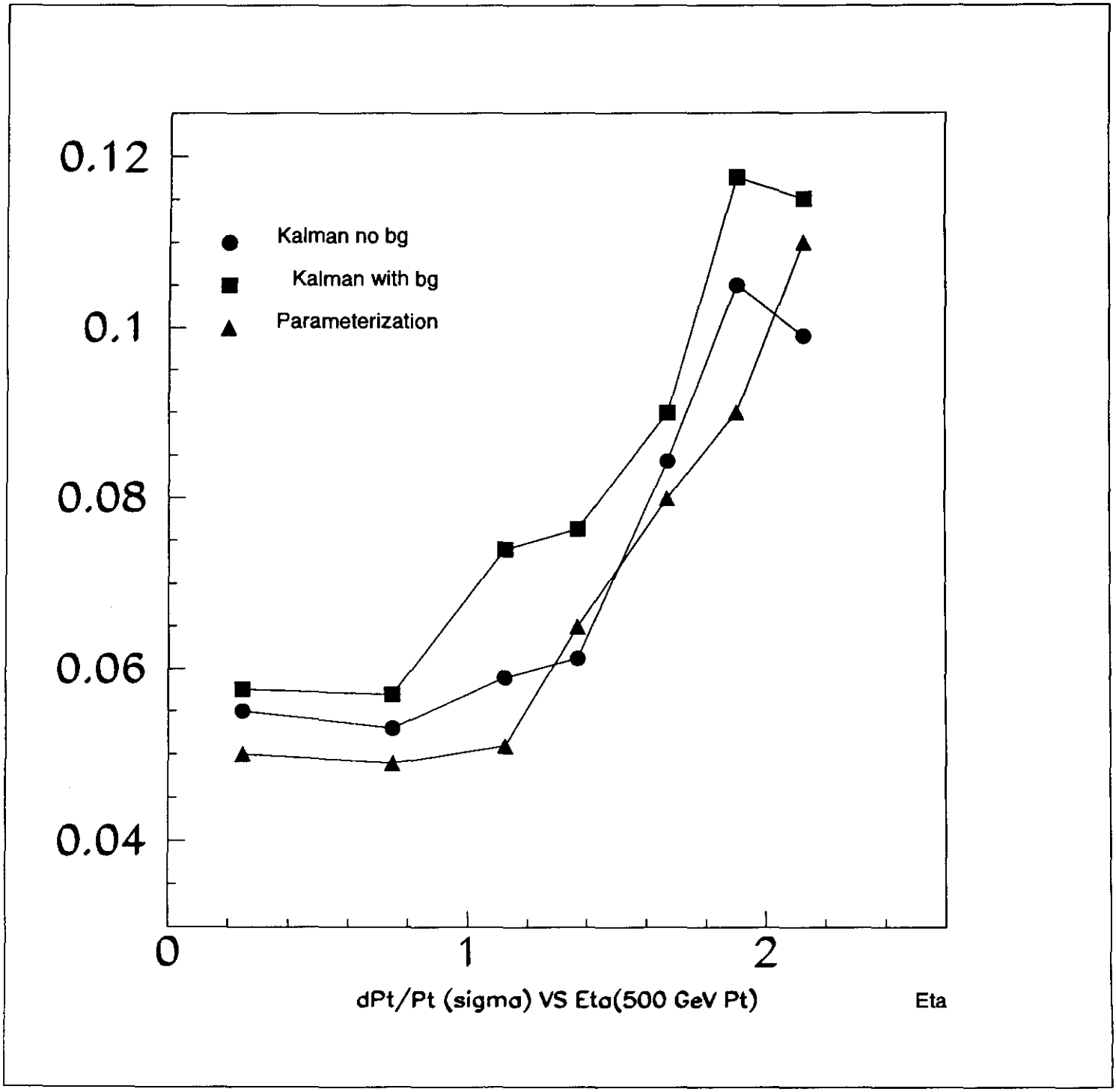

Figure 17) Track resolution plot as a function of η for the 500 GeV P_t muon sample using the Kalman Filter .

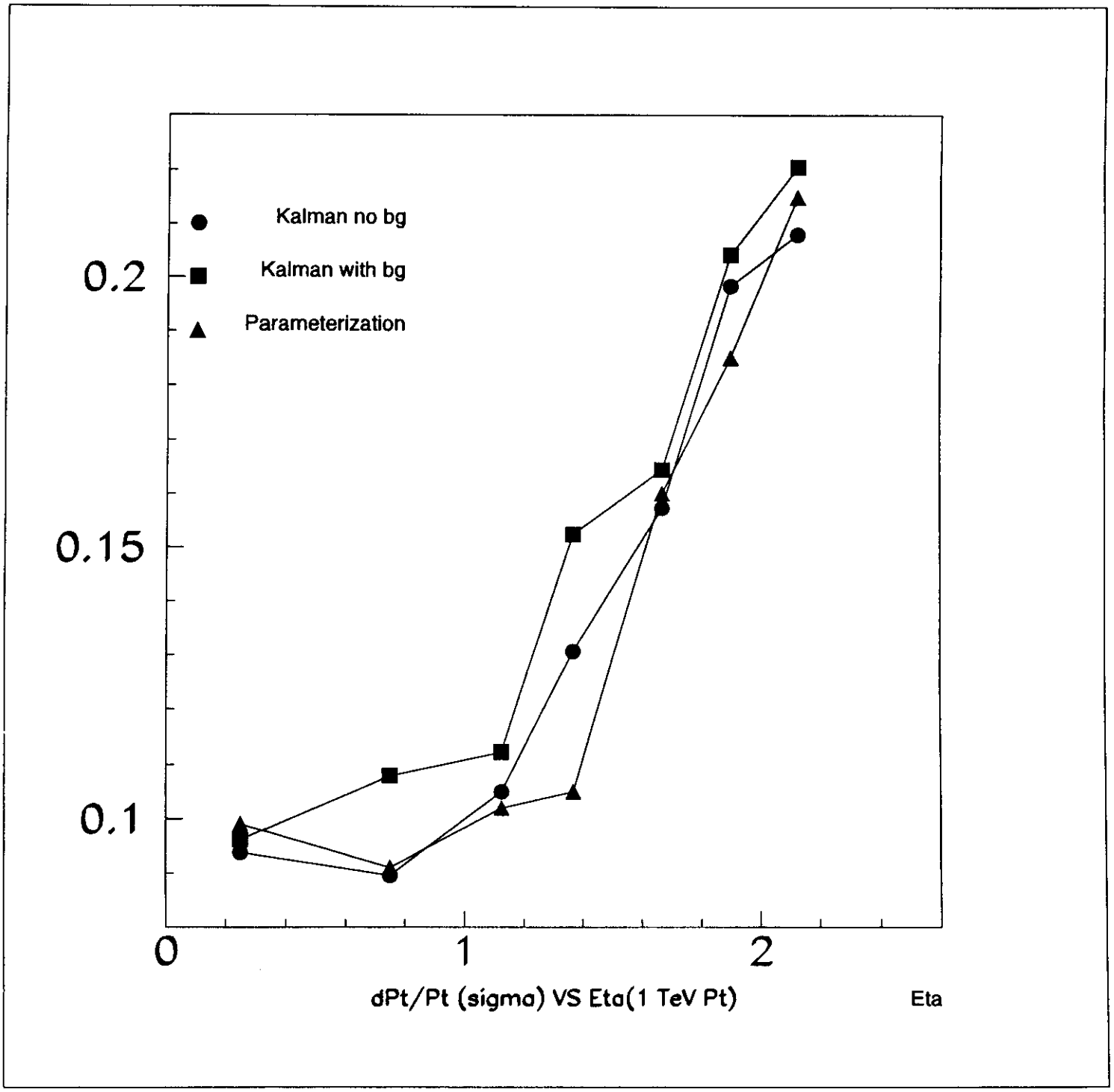

Figure 18) Track resolution plot as a function of η for the 1 TeV P_t muon sample using the Kalman Filter .

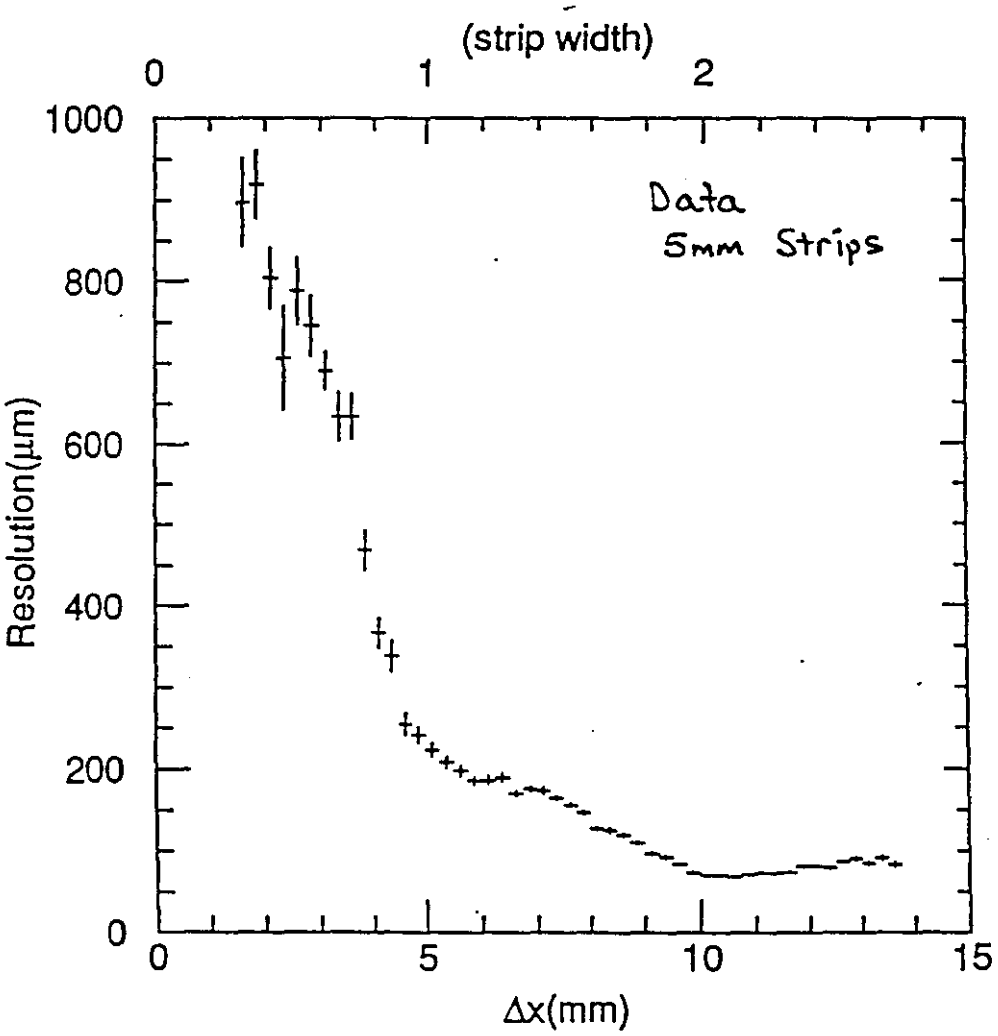

Figure 19) Chamber resolution of a charged hit in the presence of another charged hit as a function of the distance between the two hits, defined as the "Two Track Resolution" in the text.

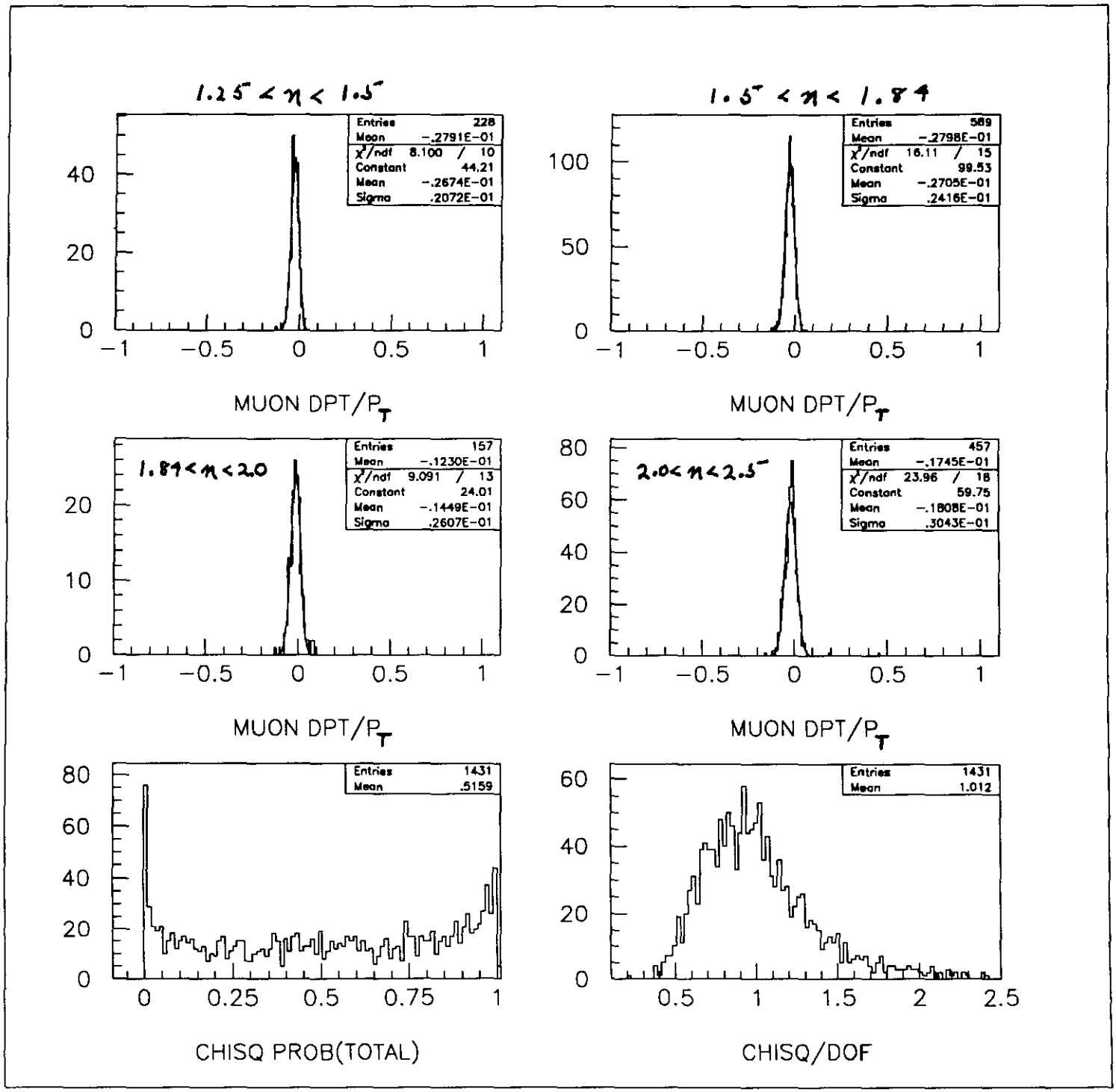

Figure 20) Track resolution distributions and quality of fit for the structure-free 100 GeV P_t sample of muons in the endcap. This sample of muon events scanned the detector in η but not in ϕ in order to access the effect of the staggering of chambers in ϕ and of chamber supports.